

Non-parametric decompositions of disk galaxies in S⁴G using DiskFit

C. Lewis,¹ K. Spekkens,^{1,2}

¹Department of Physics, Engineering Physics and Astronomy, Queen’s University, Kingston, ON K7L 3N6, Canada

²Department of Physics and Space Sciences, Royal Military College of Canada, PO Box 17000, Station Forces, Kingston, ON K7K 7B4, Canada

Accepted XXX. Received YYY; in original form ZZZ

ABSTRACT

We present photometric models of 532 disk galaxies in 3.6 μ m images from the Spitzer Survey of Stellar Structure in Galaxies (S⁴G) using the non-parametric DISKFIT algorithm. We first test DISKFIT’s performance on 400 synthetic S⁴G-like galaxy images. DISKFIT is unreliable in the bulge region, but accurately disentangles exponential disks from Ferrers bars farther out as long as their position angles differ by more than 5°. We then proceed to model the S⁴G galaxies, successfully fitting 489 of them using an automated approach for initializing DISKFIT, optimizing the model and deriving uncertainties using a bootstrap-resampling technique. The resulting component geometries and surface brightness profiles are compared to those derived by Salo et al using the parametric model GALFIT. We find generally good agreement between the models, but discrepancies between best-fitting values for individual systems are often significant: the choice of algorithm clearly impacts the inferred disk and bar structure. In particular, we find that DISKFIT typically assigns more light to the bar and less light to the disk relative to the Ferrers and exponential profiles derived using GALFIT in the bar region. Given DISKFIT’s reliability at disentangling these components in our synthetic images, we conclude that the surface brightness distributions of barred S⁴G galaxies are not well-represented by these functional forms. The results presented here underscore the importance of validating photometric decomposition algorithms before applying them to real data and the utility of DISKFIT’s non-parametric approach at measuring the structure of disks and bars in nearby galaxies.

Key words: galaxies: photometry - galaxies: structure - galaxies: bulges - galaxies: spiral

1 INTRODUCTION

Secular processes dominate the evolution of galaxies at low redshifts, with galactic bars being among the main mechanisms driving evolution (e.g. Kormendy & Kennicutt 2004; Kormendy 2013; Athanassoula 2013; Sellwood 2014). Bars are long-lived features, initially formed as elongated gravitational instabilities in the plane of the galaxy disk (e.g. Hohl 1971; Sellwood 1981; Binney & Tremaine 1987). As the instability grows and the bar gets stronger it will increase in length and trap more disk stars. This takes angular momentum from the bar, making it thinner and decreasing its rotational pattern speed (Athanassoula 2003). Absorption of angular momentum by the halo also strengthens the bar (Athanassoula 2002, 2003). Additionally, bars dissipate angular momentum via gas in the disk, channelling it toward the centre of the galaxy and triggering central star formation (Englmaier & Gerhard 1997; Athanassoula 1992; Sellwood

2013; Tonini et al. 2016). The physical properties of bars are therefore important indicators of the evolutionary states of their host galaxies (Pérez et al. 2017; Kruck et al. 2018; Hoyle et al. 2011; Masters et al. 2011; Athanassoula et al. 2013).

Over the years, a variety of techniques have been adopted to extract bar properties from photometric images of nearby galaxies. Initial attempts focused on applying parametric functions to one-dimensional surface brightness profiles derived by fitting isophotal ellipses (e.g. Kormendy 1977a,b,c; Kent 1985; Burstein 1979), and changes in the ellipticity and position angle of the ellipses themselves can also be used to characterize bars (Wozniak et al. 1995; Erwin 2005). However, tests show that the latter approach leads to systematic biases in the resulting bar lengths (Gadotti 2008; Aguerri et al. 2009), while significant parameter degeneracies can emerge from the former approach, particularly near the galaxy centre (e.g. MacArthur et al. 2003; Kormendy 1977b).

2 Lewis & Spekkens

More recently, applying two-dimensional models directly to the imaging data has become the norm for characterizing bars. Several algorithms (e.g. BUDDA, de Souza et al. 2004; GIM2D, Marleau & Simard 1998; Simard et al. 2002; IMFIT, Erwin 2015; GALFIT/GALFITM, Peng et al. 2002, 2010; Vika et al. 2013) decompose galaxy images into parametrized disks, bars, and bulges, and more complex structural components such as arms and rings can also be incorporated (Peng et al. 2010; Ma et al. 2017; Muthu Pakdil et al. 2017). The reliability and uniqueness of these models is hard to infer, however, since many algorithms don't return uncertainties on best-fitting values. Bar parameters are thus often presented without uncertainties (Weinzirl et al. 2008; Salo et al. 2015; de Swardt et al. 2015). Although modelling large galaxy samples is an effective means of minimizing the statistical uncertainties on measured values (Blanton et al. 2005), detailed survey- and algorithm-specific tests are required to determine whether or not systematic biases are important (Schombert & Bothun 1987; Byun & Freeman 1995; Wadadekar et al. 1999; MacArthur et al. 2003; Gadotti 2008; Peters & Kuzio de Naray 2017).

DISKFIT is an algorithm for modelling two-dimensional velocity maps or images of nearby disk galaxies (Spekkens & Sellwood 2007; Sellwood & Spekkens 2015; Kuzio de Naray et al. 2012). It was designed to measure the kinematic and photometric properties of asymmetries in these systems and to generate robust uncertainties of the best-fitting values using a bootstrap-resampling technique (Sellwood & Sánchez 2010). In the uncertainty estimation, the residuals from a best-fitting model are randomly scrambled and added to the model to create each bootstrap realization. The standard deviation of the best fitting model values from the ensemble of realizations is then adopted as the uncertainty (Spekkens & Sellwood 2007). The photometric side of the code differs from many other approaches in that it models the surface brightness distribution of the disk and bar – each assumed to have a fixed centre, position angle and ellipticity – non-parametrically. DISKFIT is therefore particularly useful for characterizing the properties of barred galaxies whose bar and disk light distributions may differ from the standard Ferrers and exponential forms, respectively, as suggested both theoretically and observationally in recent studies (Gadotti 2008; Kim et al. 2016b; Williams & Evans 2017).

The Spitzer Survey of Stellar Structure in Galaxies (S^4G , Sheth et al. 2010) produced $3.6\mu m$ and $4.5\mu m$ images for 2331 nearby galaxies in order to map their stellar mass distributions at wavelengths largely immune to dust contamination (Muñoz-Mateos et al. 2013; Querejeta et al. 2015; Muñoz-Mateos et al. 2015). The S^4G sample is therefore an ideal testbed for comparing the performance of different photometric decomposition models at recovering disk and bar properties. Salo et al. 2015 (hereafter S15) present multi-component “human-supervised” models of S^4G barred and unbarred galaxies using GALFIT that have been extensively used to constrain their underlying structure and evolution (Muñoz-Mateos et al. 2015; Erroz-Ferrer et al. 2015; Sorce et al. 2016; Bittner et al. 2017). S15 discuss the impact of changing the PSF, sky subtraction, weight smoothing, and model components on the best-fitting GALFIT models, and also compare to models in the literature for a subset of the sample. However, S15 do not report uncertainties on their final parameters or test GALFIT's performance on

S^4G -like imaging, and the reliability of their decompositions is therefore not quantified. Since DISKFIT's non-parametric approach to characterizing disk and bar components differs from GALFIT's parametric one, it is an ideal algorithm to compare to the S15 results to gain a better understanding of the underlying structure of nearby disks and bars and the uncertainties associated with extracting this structure from imaging data (e.g. Peng et al. 2010).

This paper presents non-parametric DISKFIT decompositions of S^4G disk galaxies for direct comparison with S15's parametric GALFIT models. Our goals are to quantitatively test DISKFIT's performance on S^4G -like imaging, to determine the conditions under which DISKFIT and GALFIT models of S^4G galaxies differ, and to explore the resulting implications for the structure of barred galaxies. §2 describes the S^4G subsample adopted for our comparison. §3 describes the synthetic galaxy images that we used to test DISKFIT on S^4G -like imaging and the corresponding modelling results. §4 presents our DISKFIT models of the S^4G subsample itself, and a comparison between the best-fitting properties of these models to the corresponding S15 GALFIT results. We discuss the implications of that comparison for the structure of nearby barred galaxies in §5.

2 SAMPLE SELECTION

There are 2331 galaxies in S^4G (Sheth et al. 2010), encompassing all morphological types. Very early and late type galaxies tend not to have distinct disks, and are not well represented by DISKFIT's models. We therefore include only rotationally supported spirals (Hubble types 0 through 7) in our subsample, as listed in the S^4G catalogue (Sheth et al. 2010). Since our focus is the characterization of bars in nearby, well-resolved disk galaxies, we exclude high inclination systems ($\epsilon_{Disk} > 0.7$) and low-quality images (quality flag $q < 4$ from S15), and require that the scale length of the disk measured by S15 be spanned by at least 15 pixels (1 pixel = 0.75 arcseconds; Sheth et al. 2010). The S^4G subsample that meets these selection criteria contains 570 galaxies, some of which are listed in Table 1 (the full table is shown in digital appendix Table A1). We fit the same $3.6\mu m$ S^4G images as modelled by S15. Figure 1 shows the distribution of morphological types included in the subsample, and Figure 2 shows the distribution of structural parameters in that subsample inferred from the GALFIT models of S15.

3 FITTING OF SYNTHETIC GALAXIES

Validating the performance of a photometric decomposition algorithm on synthetic galaxies before proceeding to interpret fits to real data is essential for disentangling physical effects from software limitations. In this section we describe the simulated S^4G -like galaxy images that we use to test DISKFIT's performance (§3.1), as well as the implications of our DISKFIT model results on our fitting procedure for real galaxies (§3.2).

Name (1)	Model (2)	Disk PA [°] (3)	ϵ_{Disk} (4)	Bar PA [°] (5)	ϵ_{Bar} (6)	Disk % (7)	Bar % (8)	flags (9)
ESO012-010	dbar	151(1)	0.62(0.02)	24(3)	0.44(0.04)	88(1)	12(1)	
ESO013-016	dbar	N/A	N/A	N/A	N/A	N/A	N/A	a
ESO026-001	dbar	45(14)	0.25(0.07)	71(1)	0.77(0.02)	92(1)	7.6(1.3)	b
ESO027-001	bdbar	93(8)	0.22(0.06)	53(2)	0.65(0.05)	82(3)	12(3)	
ESO027-008	d	145(2)	0.64(0.02)	N/A	N/A	N/A	N/A	b
...								
UGC09951	d	~ 120	~ 0.36	N/A	N/A	N/A	N/A	c d
UGC10020	d	N/A	N/A	N/A	N/A	N/A	N/A	c f
UGC10437	d	167(4)	0.18(0.03)	N/A	N/A	N/A	N/A	c
UGC10445	bd	124(3)	0.32(0.03)	N/A	N/A	98(2)	N/A	
UGC12707	dbar	43(3)	0.46(0.03)	65(2)	0.72(0.03)	86(2)	14(2)	b

Table 1. Galaxies in S⁴G subsample. Column 1 is the galaxy name, column 2 indicates the model used in DISKFIT (b=bulge, d=disk, and bar), column 3 is the position angle of the disk in degrees (numbers in parentheses are the uncertainties on the reported values), column 4 is the ellipticity of the disk ($1 - b/a$), column 5 is the position angle of the bar in degrees, column 6 is the bar ellipticity, column 7 is the fraction of the model light in the disk, column 8 is the fraction of the model light in the bar, and column 9 is the fit flag. The fit flags are a: Excluded galaxies with $|PA_{Disk} - PA_{Bar}| < 5^\circ$. b: Nucleus included in GALFIT fit, but not in DISKFIT fit. c: Two disks fit in GALFIT, one disk fit in DISKFIT. d: Galaxies for which the only model that we could fit was disk-only, with fewer surface brightness rings than used in other DISKFIT fits. e: Galaxies for which we fit the same components as in the GALFIT fits, with fewer surface brightness rings than used in other DISKFIT fits. f: Galaxies for which GALFIT parameters used as DISKFIT inputs caused the DISKFIT minimization to fail. The full table is shown in the digital appendix Table A1.

3.1 Setup and Fitting Procedures

We draw from the statistical properties of the subsample galaxies obtained from the fourth data reduction pipeline of S⁴G (S15) to create 400 images of synthetic galaxies, each containing a disk, a bar, and a bulge. The goal is to simulate galaxies with idealized structural components and image properties similar to the S⁴G galaxy subsample in order to quantitatively assess DISKFIT’s performance in this regime. For simplicity we adopt parametric surface brightness profiles for the synthetic galaxies, even though DISKFIT recovers them non-parametrically.

We adopt exponential surface brightness profiles for the simulated disks:

$$\Sigma_{disk}(r) = \Sigma_{0,disk} e^{(-r/r_d)}, \quad (1)$$

with a disk scale length r_d , and a central surface brightness $\Sigma_{0,disk}$. The simulated surface brightness distribution of the bar is given by the Ferrers function (Ferrers 1877):

$$\Sigma_{bar}(r) = \begin{cases} \Sigma_{0,bar} [1 - (r/r_{bar})^2]^2 & r < r_{bar} \\ 0 & r \geq r_{bar} \end{cases} \quad (2)$$

with a truncation radius r_{bar} , and a central surface brightness $\Sigma_{0,bar}$. Finally, we adopt a Sérsic function (Sérsic 1963) for the simulated bulges:

$$\Sigma_{bulge}(r) = \Sigma_{eff} \exp \left(-b_n \left[\left(\frac{r}{r_{eff}} \right)^{1/n} - 1 \right] \right), \quad (3)$$

with a Sérsic index n , and surface brightness Σ_{eff} at effective radius r_{eff} . We use the approximation $b_n = 1.99n - 0.327$ (Capaccioli 1989).

The component parameters in the simulated galaxy images are randomly drawn from their distributions in the S⁴G subsample as determined by S15, so that the real and synthetic samples span comparable ranges. The histograms in Figure 2 show the distribution of r_d , ϵ_{Disk} , Σ_{disk} , $r_d - r_{bar}$, $\epsilon_{Disk} - \epsilon_{Bar}$, and $\Sigma_{disk} - \Sigma_{bar}$ in the sample of synthetic

galaxies. We also draw from the S⁴G distributions for the bulge parameters r_{eff} , ϵ_{Blg} and n , imposing constraints on the relative surface brightnesses of the bulge and disk based on ranges from S15.

Once the structural properties of each galaxy are selected, the simulated images are made to be photometrically similar to those of the S⁴G subsample. We convolve the synthetic images using a Gaussian with full width at half maximum FWHM = 2.1 arcsec (with 0.75 arcsec/px), which closely resembles the IRAC PSF (Sheth et al. 2010). We add Poisson noise to the Gaussian-convolved images to mimic the source and sky background-dominated noise in the S⁴G images (Sheth et al. 2010). We also create uncertainty maps for each galaxy using an algorithm similar to that adopted by S15. Examples of simulated galaxy images are shown in Figure 3.

After the creation of the synthetic sample, we apply DISKFIT to each simulated galaxy and its corresponding uncertainty map. We fit disk, bar, and bulge models for all systems. Input guesses for the disk PA, bar PA, ϵ_{Disk} , ϵ_{Bar} , Sérsic n , ϵ_{Blg} and r_{eff} are taken to be their true values in order to maximize the chances of recovery. We initially allow all parameters to vary freely in the models to determine the best fitting non-parametric surface brightness profiles for the disk and the bar. However, for reasons that we discuss in §3.2 we leave Sérsic n fixed to the true value for all figures following Figure 4. We set DISKFIT to correct for seeing using the same Gaussian PSF as adopted in the simulations. We estimate uncertainties on the fitted parameters using 20 bootstrap-resampled realizations of each model using the radial-rescaling method of Sellwood & Sánchez (2010), where the number of bootstrap realizations is limited by the computing resources available through the Centre for Advanced Computing (CAC) at Queen’s University. The next section presents the results of these fits.

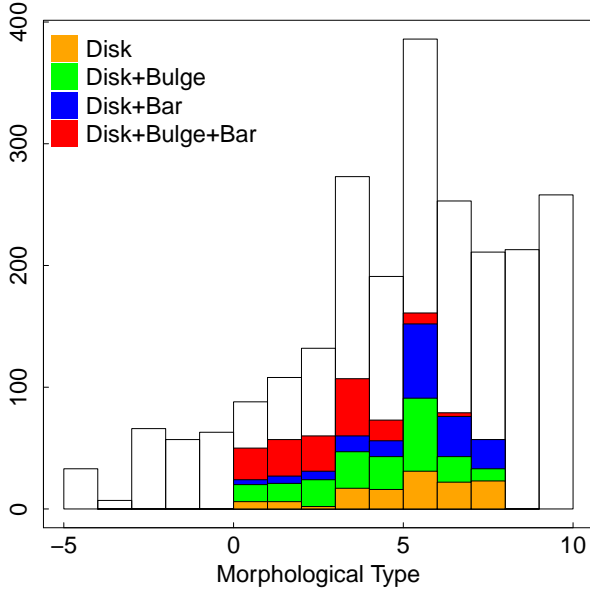


Figure 1. Distribution of morphological types included in the S⁴G subsample modelled with DISKFIT (coloured bars), compared to that of all S⁴G galaxies (open bars). The coloured bars show subsample galaxies with different structural components as determined by the GALFIT models of S15: the orange histogram represents galaxies that have a only a disk, the green histogram represents galaxies that have a disk and a bulge, the blue histogram represents galaxies that have a disk and a bar, and the red histogram represents galaxies that have a disk, a bar, and a bulge.

3.2 Results of Synthetic Galaxy Fits

Figure 4 shows the relationship between the input and recovered bulge properties for the synthetic galaxy images. Panels a), b) and c) show the bulge properties recovered when all bulge parameters are allowed to vary in the fits. It is clear that Sérsic n is not reliably recovered, and that there is significant scatter between the input and recovered $\epsilon_{B\text{lg}}$ and r_{eff} . The situation improves when Sérsic n is fixed to the input value, as shown in panels d) and e) in Figure 4. The recovered values for r_{eff} are scattered symmetrically about the 1:1 relation. The recovered $\epsilon_{B\text{lg}}$ loosely follows the 1:1 line, with the majority of recovered values underestimating the true ones: this is a consequence of DISKFIT assigning bulge light to the (non-parametric) disk. The fraction of light in the bulge (a cumulative measure computed from n , $\epsilon_{B\text{lg}}$ and r_{eff}) is not recovered by DiskFit regardless of whether or not n is held fixed.

Our simulations imply that DISKFIT cannot reliably recover Sérsic n in S⁴G-like imaging, i.e simulated galaxy images in which the range of structural parameter values, the resolution, and the image noise resemble that of S⁴G. We therefore fix this parameter in all subsequent DISKFIT models of both simulated and real systems, and have used our simulations to verify that the disk and bar properties are unaffected by this choice beyond the bulge region. Figures 4d) and 4e) imply that, even with n fixed to the correct value, the other Sérsic bulge properties are not well-recovered. It

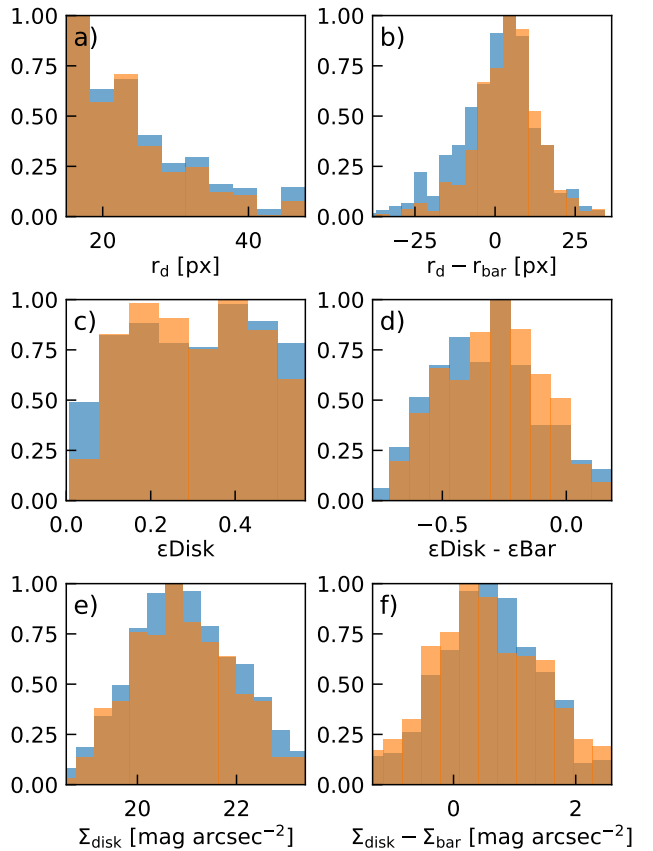


Figure 2. Distributions of: a): disk scale length, b): difference between disk scale length and bar radius, c): disk ellipticity, d): difference between disk and bar ellipticity, e): disk central surface brightness, f): difference between the central surface brightnesses of the disk and bar for the S⁴G subsample (blue) histograms and the simulated galaxy images (orange).

is therefore likely that the DISKFIT models of the S⁴G subsample (where the true n is unknown) are unreliable in the bulge region of each galaxy, and we do not consider this region further here. All subsequent models of synthetic and real galaxies keep n fixed.

A comparison between the input and recovered position angles and ellipticities of the disk and bar in our synthetic galaxy images is shown in Figure 5 and the best fitting values from least-squares linear fits to each trend are given in Table 2. Panels a) and b) of Figure 5 show that for the vast majority of simulated galaxies, the disk and bar PAs are accurately and precisely recovered by DISKFIT. We note that synthetic galaxies with outlying values of the recovered disk PA are mostly low-inclination systems with $\epsilon_{\text{Disk}} < 0.1$. The relationships between the input and recovered disk and bar ellipticities in Figures 5c) and 5d) show comparatively more scatter, but the correlations remain strong. Table 2 shows that the median absolute deviation normalized to equal the standard deviation for Gaussian distributions (MAD/1.4826) about the best-fitting linear relationship implies an extremely small scatter of the best fitting values from their true ones for most synthetic galaxy fits.

Insight into the nature of the outliers can be gleaned by

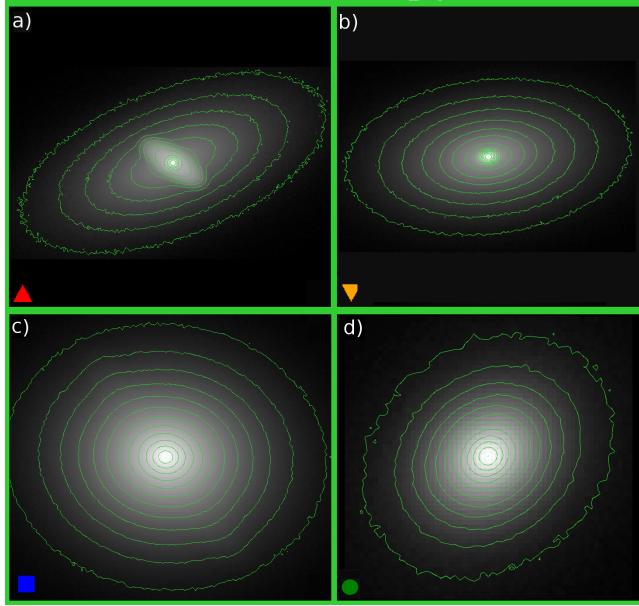


Figure 3. Simulated images of four synthetic galaxies. Each image is shown on a logarithmic scale, with 13 contour levels spaced by ~ 0.25 dex. The location of these specific synthetic galaxies in Figure 5 is given by the symbol in the bottom-left corner of each panel in this figure, and the symbol colour indicates the best fitting surface brightness profiles in Figure 6.

examining the coloured points in Figure 5, which correspond to the individual galaxies in Figure 3. The red triangles in Figure 5 show an example of a synthetic galaxy, highlighted in Figure 3a), where the recovered properties match the input values within the uncertainties; this system has a relatively bright bar ($r_{bar} = 23$ px, where the bar comprises 62% of the total galaxy light) at a distinct position angle from the underlying disk.

By contrast, the outlying green circles in Figure 5b) and 5d) illustrate DISKFIT’s higher likelihood of failing to recover a weak bar ($r_{bar} \simeq 16$ px with 0.3% galaxy light) in the synthetic galaxy in Figure 3d); this is perhaps to be expected, since the bar isn’t visible by eye. DISKFIT fares better at recovering the longer and slightly stronger bar ($r_{bar} = 56$ px with 0.9% galaxy light) in the synthetic image in Figure 3c), represented by the blue squares in Figure 5; the bar properties are well-recovered, though ϵ_{Disk} is strongly under-estimated. These individual examples illustrate that synthetic galaxies with recovered properties that deviate from the input ones tend to have one structural component that is much brighter than the others.

The yellow triangles in Figure 5, which show the recovered parameters of the synthetic galaxy in Figure 3b), illustrate how DISKFIT performs when the disk and bar PA are closely aligned (the two have identical position angles in this specific case). The Disk PA and ϵ_{Disk} are well-recovered, but ϵ_{bar} is poorly recovered and the Bar PA is completely lost.

Figure 6 compares the surface brightness profiles of the disk and the bar recovered by DISKFIT for the synthetic galaxies, where $\Delta\mu = \mu_{recovered} - \mu_{input}$ at the discrete radii selected during modelling. Points with $\Delta\mu > 0$ there-

fore correspond to an overestimation of the light profile by DISKFIT, and points with $\Delta\mu < 0$ correspond to an underestimation. We normalize the radial axes by r_d and r_{bar} of the (parametrically-constructed) input synthetic galaxies for convenience, but emphasize that these quantities have no meaning in the DISKFIT context since the disk and bar are modelled non-parametrically.

The narrow interquartile range of $\Delta\mu$ (red shaded regions) in Figure 6a) shows that in general, for $0.5 < r/r_d < 3$, exponential disk surface brightness profiles are reliably recovered non-parametrically by DISKFIT. At smaller r , the disk and bar surface brightnesses are not well-recovered due to confusion with the bulge (which itself isn’t reliably modelled; see Figure 4). Note that the extreme outliers here consist of galaxies similar to those shown in Figure 3b) - 3d) (coloured yellow, blue, and green in Figures 5 and 6 respectively), where the disk-bar degeneracies are hardest to break. Figure 6b) shows that the bar is also reliably recovered by DISKFIT in the range $0.2 < r/r_{bar} < 0.8$. Note that because DISKFIT models the surface brightness profiles of the disk and bar non-parametrically, the two components become degenerate in the model when their position angles are aligned and their ellipticities are similar. This is clearly illustrated by the yellow lines in Figure 6, which show the best-fitting profiles corresponding to the synthetic galaxy in Figure 3b). Our simulations suggest that, for intermediate-inclination disks, DISKFIT is unreliable at distinguishing the disk and bar components when $\Delta PA = |PA_{disk} - PA_{bar}| \lesssim 5^\circ$ (see Holmes et al. 2015 and Randriamampandry et al. 2016 for similar findings in kinematic DISKFIT models). Finally, for $r/r_{bar} > 0.85$, the noise in DISKFIT’s recovery of the bar increases as the bar light fades sharply (in the Ferrers profile, the bar fades by ~ 7 mag arcsec $^{-2}$ for $0.85 < r/r_{bar} < 1$).

The outcome of our DISKFIT modelling of the simulated galaxies has important implications for our models of the S⁴G subsample described in §4.1. We find that bulge properties are not reliably modelled. However, the position angles, ellipticities and surface brightness profiles of galaxies with exponential disks and relatively long, relatively bright Ferrers bars (usually those at least barely distinguishable by eye) are well-recovered beyond the bulge region. The notable exception to these criteria are systems where the disk and bar position angles lie within 5° of one another, which may cause degeneracies in DISKFIT’s non-parametric models.

4 FITTING OF S⁴G GALAXIES

We now proceed to model the S⁴G subsample listed in Table 1 with DISKFIT, in order to compare the resulting components with those obtained from the human-supervised application of GALFIT by S15. We use the synthetic galaxy models of §3 to guide the selection of subsample galaxies that we attempt to fit (§4.1), as well as to interpret our results (§4.2).

4.1 Setup and Fitting Procedures

For each system in our subsample, we fit for the same combination of disk, bar, and/or bulge as included in the final GALFIT decomposition presented by S15. The components included in each of the models are listed in column 2 of Table 1.

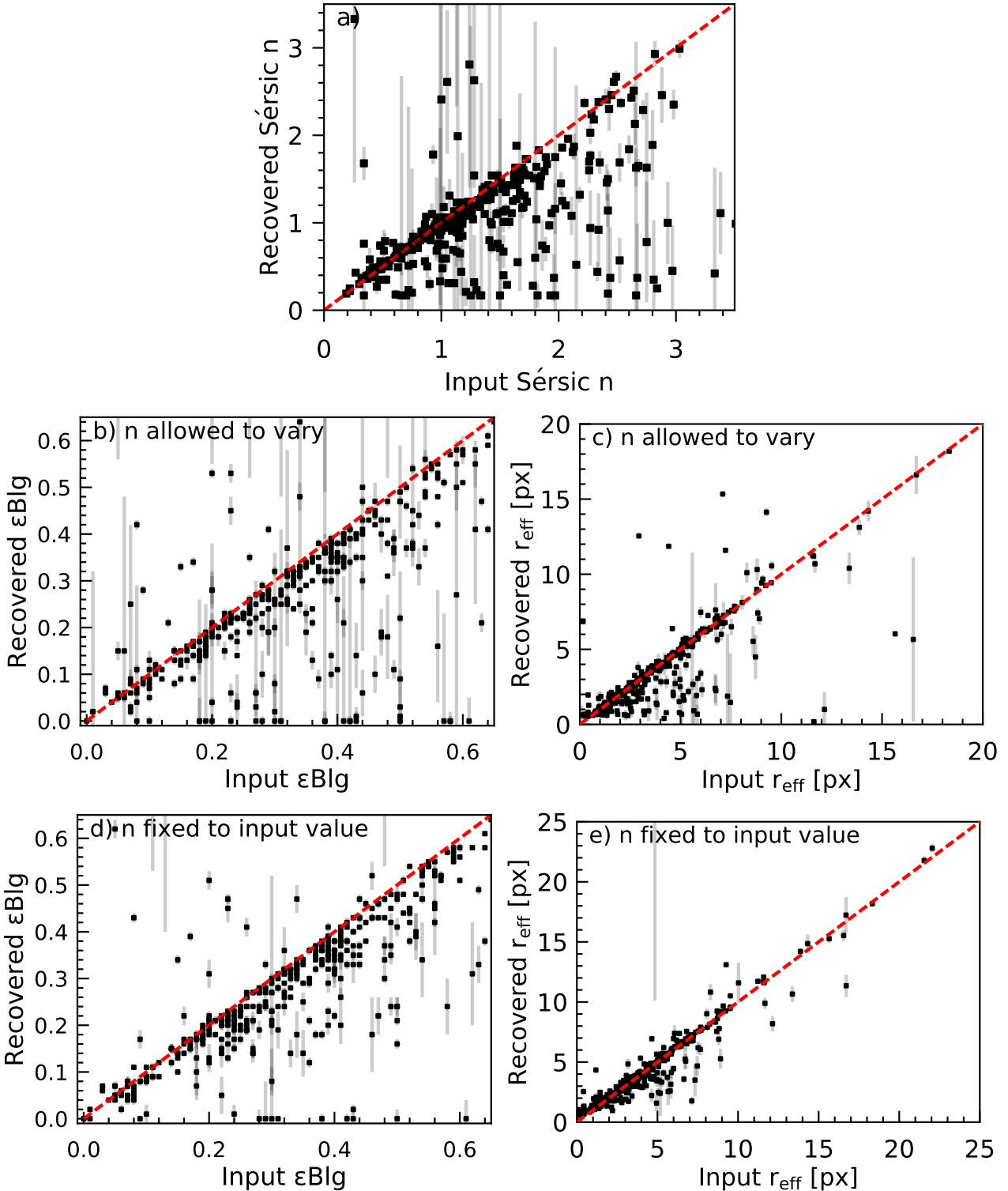


Figure 4. Recovered vs input bulge properties from DISKFIT fits to synthetic galaxies: **a)**: Sérsic n , **b,d)**: bulge ellipticity, **c,e)**: bulge effective radius. In **b**) and **c**), Sérsic n is allowed to vary, while in **d**) and **e**) n is fixed to the true value. In each plot, the dashed red line is the 1:1 relationship.

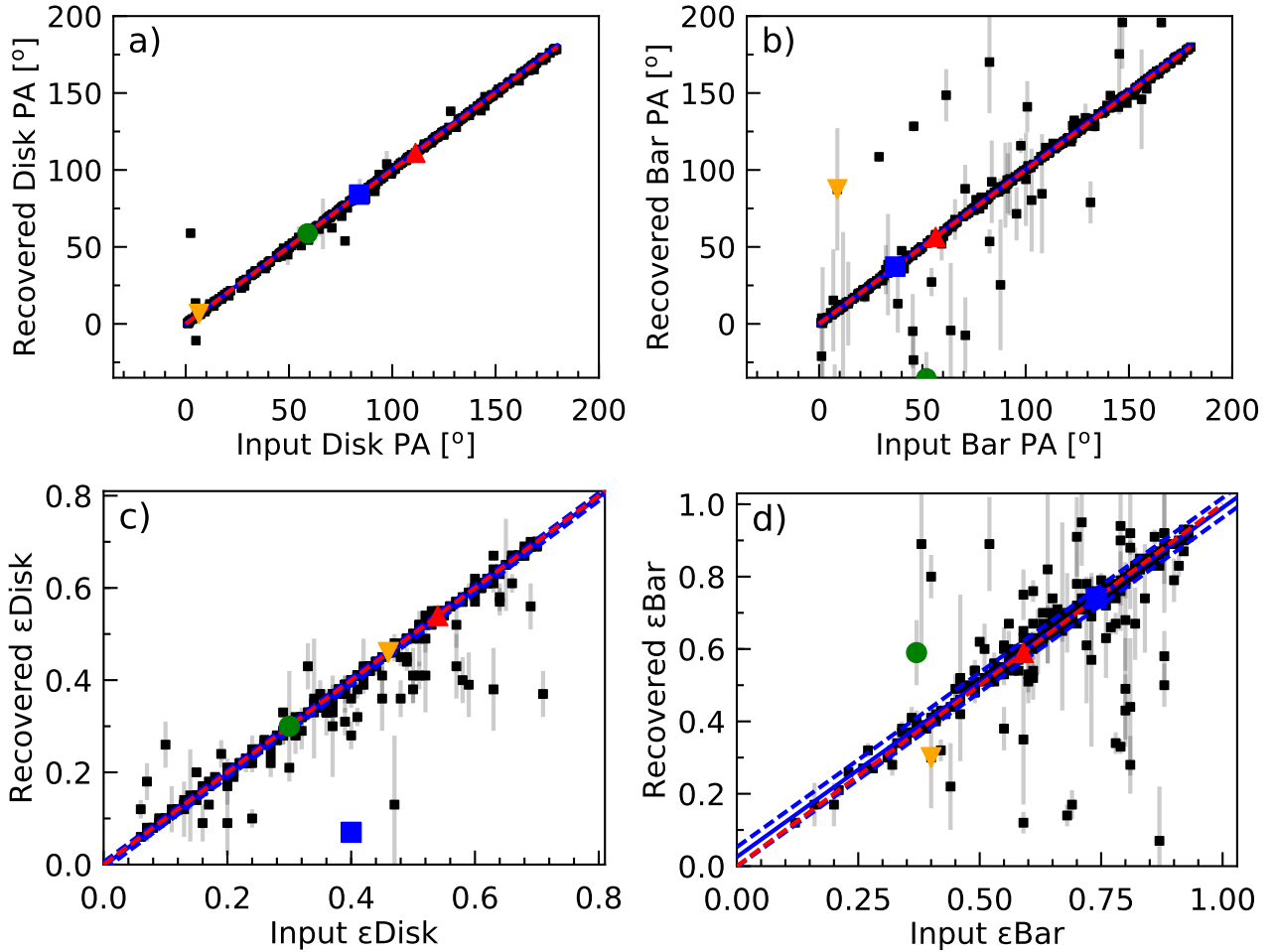


Figure 5. Recovered vs input disk and bar from DISKFIT fits to synthetic galaxies: **a)**: disk position angle, **b)**: bar position angle, **c)**: disk ellipticity, **d)**: bar ellipticity. In each panel, the solid blue line is the best-fitting linear least squares relationship, the dashed blue lines show two times the normalized median absolute deviation (MAD/1.4826) about the best fit, and the dashed red line is the 1:1 relationship. The coloured points indicate the synthetic galaxy images shown in Figure 3.

We attempt to model most galaxies in the subsample with DISKFIT, using the disk geometry (ϵ_{Disk} , Disk PA) obtained by S15 as input guesses, as well as the S15 bar geometry (ϵ_{Bar} , Bar PA) when one is included. We use the exponential disk scale length r_d estimated by S15 to define the radii at which we solve for the surface brightness of each component, which we set to every third pixel from $r = 0$ to $r = 3r_d$, and then every fifth pixel out to $6r_d$. The best-fitting model values do not depend strongly on the adopted radial sampling cadence. We estimate uncertainties on the model parameters using 200 bootstrap realizations, a number again constrained by the computing resources available to us through the CAC. As discussed in §3.2 we will not compare models of the bulge because our simulations imply that DISKFIT is unreliable in that region. For models including a bulge, we fix Sérsic n to the S15 value and allow for r_{eff} and ϵ_{Bdg} to vary, using the best-fitting values from S15 as DISKFIT initial guesses. Parameters listed as ‘N/A’ in Table 1 were not included in the model for that particular galaxy.

The results of the fits for each galaxy in the S⁴G subsample are given in Table 1, and the data files containing

the resulting surface brightness profiles are available in the electronic version of the paper.

The simulations of §3.2 imply galaxies with $|Disk PA - Bar PA| \lesssim 5^\circ$ are not reliably modelled by DISKFIT. We preemptively exclude the 38 S⁴G subsample galaxies for which this is the case in the S15 models, listing them in Table 1 with flag ‘a’. We therefore attempt to fit a total of 532 galaxies. We note that some GALFIT models include a nuclear component (144 galaxies) or a second disk (89 galaxies), which we do not include in the DISKFIT models; these systems are flagged with a ‘b’ or ‘c’ in the last column of Table 1, respectively.

Additionally, there are a few galaxies for which we struggled to recover the same components as those found by S15 using GALFIT, with DISKFIT getting ‘hung up’ in parameter space during the minimization or after the first few bootstraps. We are able to recover the GALFIT morphology for some of these systems when we reduce the number of rings used in the DISKFIT surface brightness profile to every fifth pixel from $r = 0$ to $r = 3r_d$, and then every tenth pixel out to $6r_d$. We give these 19 galaxies an ‘e’ flag in Table 1. For other galaxies that we struggle to fit with the same process,

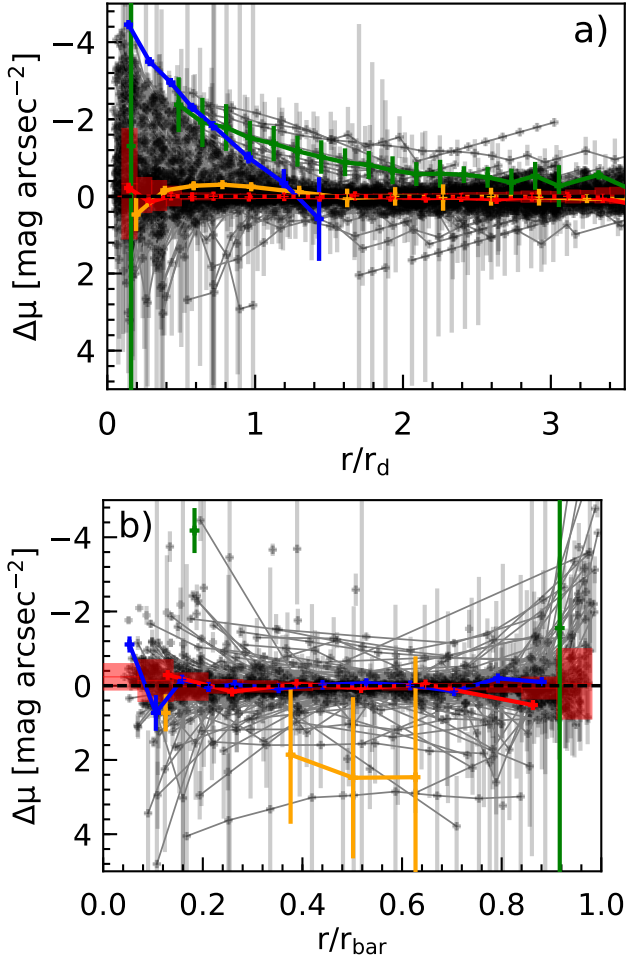


Figure 6. Difference between the recovered (non-parametric) and input (parametric) surface brightness profiles of a): the disk and b): the bar measured by DISKFIT from the simulated galaxy images, where $\Delta\mu = \mu_{\text{recovered}} - \mu_{\text{input}}$. Connected points belong to the same galaxy, and the radial range has been normalized to the input r_d and r_{bar} , respectively. The dashed black line indicates $\Delta\mu = 0$, and red rectangles indicate the interquartile range. The coloured lines correspond to the best-fitting profiles to the synthetic galaxy images with same-coloured symbols in Figure 3.

we are able to fit a disk-only model (reporting approximate values), again using fewer surface brightness rings. These 8 galaxies are listed in Table 1 with flag ‘d’. Finally, there are 16 galaxies for which we were not able to use GALFIT parameters as input at all, with DISKFIT failing to minimize for even disk-only models. We flag these galaxies with an ‘f’ in Table 1, and return to them in §5. We omit the S⁴G subsample galaxies with flags ‘a’, ‘d’, ‘e’, and ‘f’ from our comparisons with the results of S15. This ‘comparison sample’ includes 489 members.

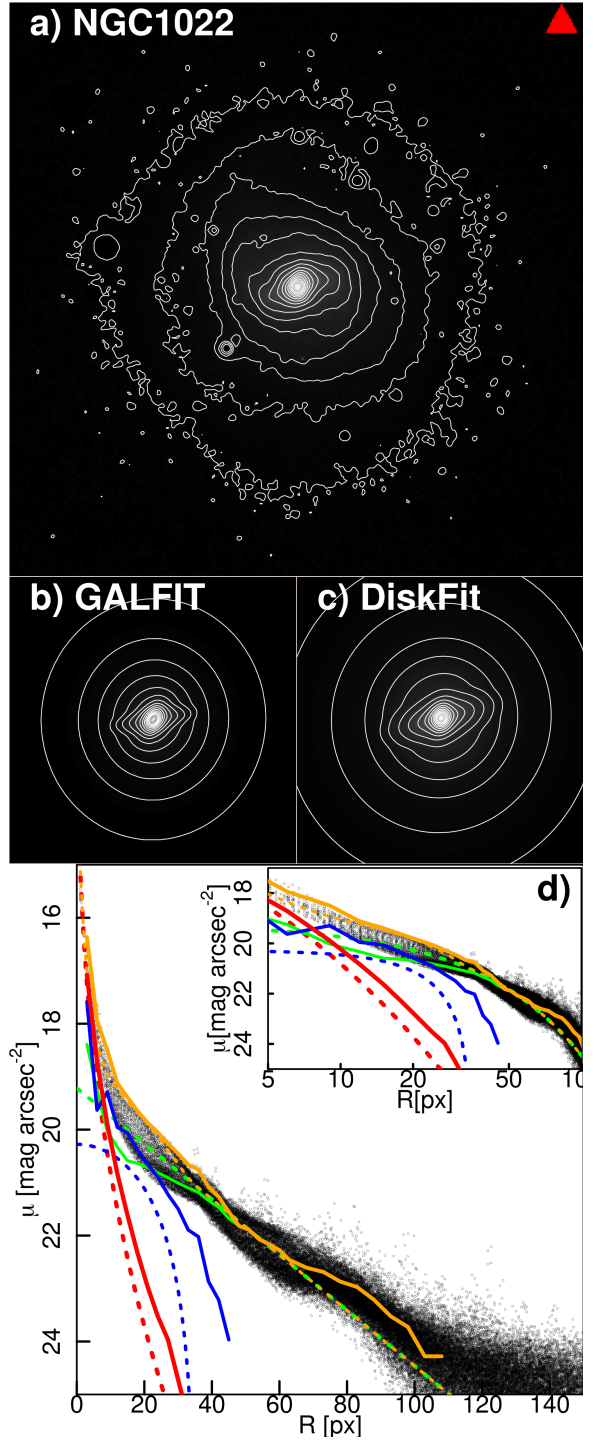


Figure 7. Images of a): NGC1022 from S⁴G, b): the S15 GALFIT model of NGC1022, and c): the DISKFIT model of NGC1022 on the same angular scale. There are 20 contours separated by ~ 0.16 dex. In the surface brightness profiles in d), the bulge model is shown in red, the bar model is shown in blue, the disk model is shown in green, and the full model is shown in yellow. The DISKFIT fit is shown with solid lines and the GALFIT fit is shown with dashed lines. Both the DISKFIT and GALFIT curves show surface brightness as a function of isophotal semi-major axis. The black dots show the surface brightness vs. sky distance from the centre of the image. NGC1022 is an example of a comparison sample with similar DISKFIT and GALFIT fits.

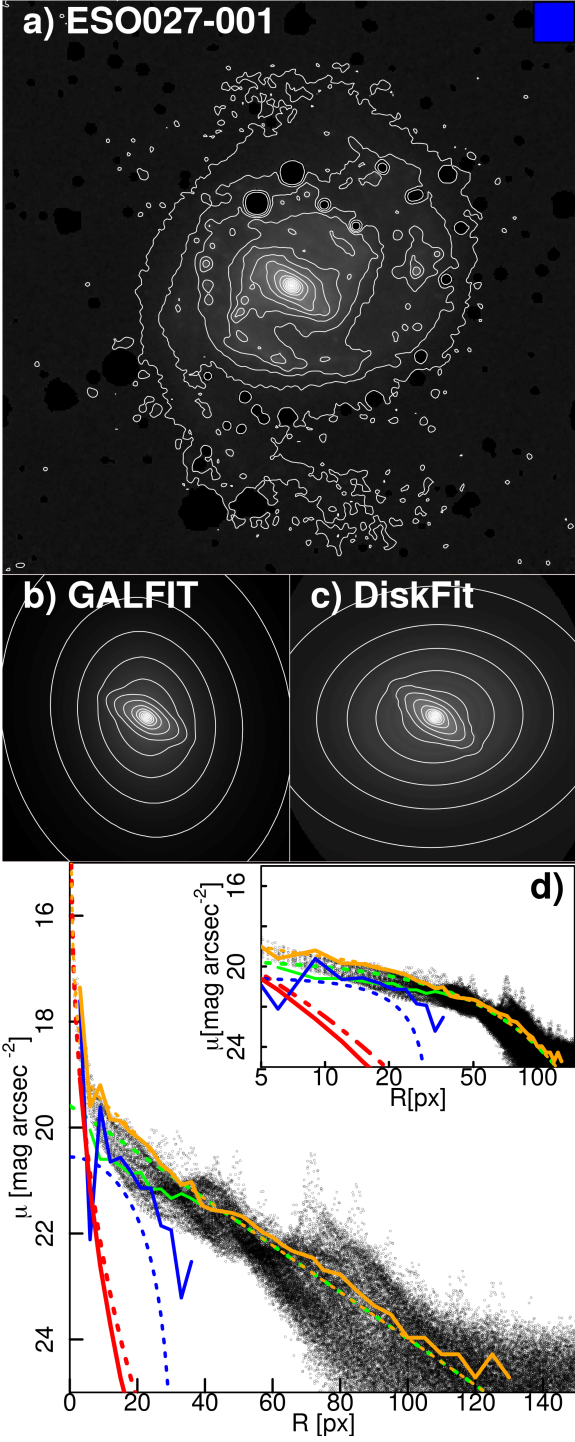


Figure 8. Same as in Figure 7, but for ESO027-001. ESO027-001 is an example of a comparison sample galaxy with significantly different disks recovered between the two algorithms.

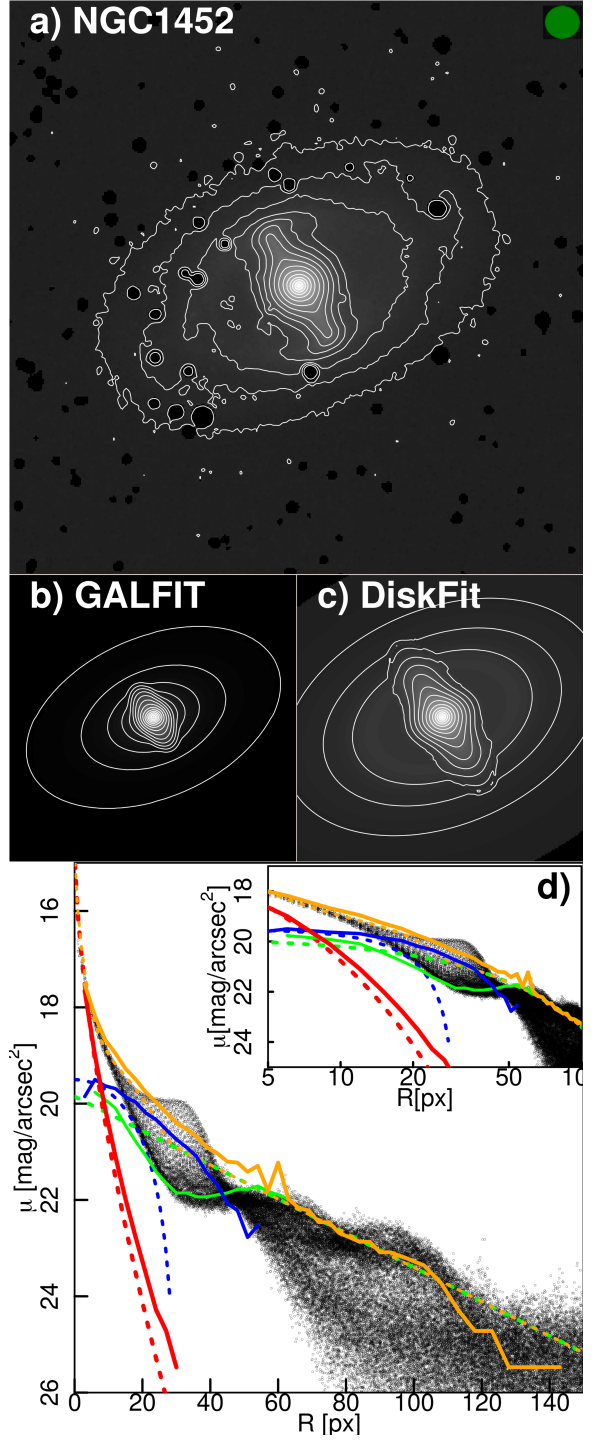


Figure 9. Same as Figure 7, but for NGC1452. NGC1452 is an example of a comparison sample galaxy with significantly different bars recovered between the two algorithms. Note that the bar length was held fixed in the GALFIT model for this galaxy (S15).

4.2 Fits to Real Galaxies: Comparing DiskFit and GALFIT

This section focuses on comparing the best-fitting DISKFIT models of the comparison sample to those adopted by GALFIT in S15. As explained in §4.1, we include the same model components as in the S15 decompositions and use their best fitting values as input guesses for DISKFIT. We therefore expect the resulting DISKFIT models to resemble the GALFIT ones as much as possible given the differences in modelling approach.

Figures 7–9 show representative examples of fits to individual galaxies, while Figures 10 and 11 examine the results for the comparison sample as a whole. Since no uncertainties on the S15 models are available, Figure 10 shows only vertical error bars while those in Figure 11 only account for DISKFIT uncertainties. For comparison sample galaxies modelled with two disks by S15, we plot the properties of one with the largest r_{eff} in Figure 10. We have verified that the properties of galaxies with nuclear components or second disks (flags ‘b’ and ‘c’ in Table 1), exhibit quantitatively and qualitatively similar behaviour in Figures 10 and 11 as the other comparison sample galaxies. Parameters of the best-fitting linear relationships between our DISKFIT fits and those adopted by S15’s models are shown in Table 2.

Figure 7 shows an example of a galaxy, NGC1022, for which the best fitting S15 GALFIT (panel b) and DISKFIT (panel c) disk-bulge-bar models closely resemble each other. The surface brightness profiles of individual components (panel d) are also similar, with DISKFIT trading some disk light (solid green line) for bar light (solid blue line) at $10\text{px} < r < 30\text{px}$ ($7.5 \text{ arcsec} < r < 23 \text{ arcsec}$) compared to GALFIT (dashed green and blue lines, respectively). NGC1022 is indicated by the red triangles in Figure 10; the DISKFIT and GALFIT disk and bar position angles and ellipticities are similar. We note that the disk ellipticities reported by S15 are derived from the shape of the outer isophotes of the images, and not by GALFIT itself. Nonetheless, we find good agreement between the DiskFit models and the S15 ones for galaxies without pronounced spiral arms, rings, or other features that are not included in the models.

Figures 8 and 9 illustrate that when such features are present in a galaxy, the best fitting S15 GALFIT and DISKFIT models can differ significantly. By construction, DiskFit uses the entire radial range of the disk to determine the PA (Spekkens & Sellwood 2007). ESO027-001 in Figure 8 has pronounced spiral arms that pull on the fits differently resulting in disks with discrepant PAs as shown by the blue squares in Figure 10. NGC1452 in Figure 9 exhibits a ring structure at the end of the bar that also produces different GALFIT and DISKFIT models, with the latter returning a much longer, brighter bar than the former with a slightly higher ϵ_{Bar} as shown by the green circles in Figure 10. We find that the photometric decompositions of galaxies with spiral arms and rings are the ones most likely to differ significantly when modelled with DISKFIT versus GALFIT.

Figure 10 shows that, on the whole, the two algorithms recover similar disk and bar geometries, with a much less centrally concentrated distribution of points than that seen in the synthetic galaxies (compare to the spread in Figure 5c) and 5d)). The trend lines are consistent with the 1:1 relations within the uncertainties (see Table 2). The agreement

between the position angles and ellipticities of the bars and disks recovered by DISKFIT and adopted by GALFIT in S15 is good for the majority of the sample galaxies. There are many more extreme outliers than that seen in the simulated sample (Figure 5a) for the disk PA, resulting in a significantly increased MAD. Many of the points that lie outside of the normalized MAD for all quantities have small error bars, indicating significantly different best-fitting models for the two algorithms (see Figure 8).

Figure 11 compares the difference between the bar and disk surface brightness profiles returned by GALFIT and DISKFIT. Here, $\Delta\mu$ represents DISKFIT’s best-fitting surface brightness profile minus the profile recovered by S15 using GALFIT: $\Delta\mu = \mu_{\text{DiskFit}} - \mu_{\text{GALFIT}}$. Points with $\Delta\mu < 0$ correspond to regions where DISKFIT attributes more light than GALFIT, and points with $\Delta\mu > 0$ correspond to regions where DISKFIT attributes less light (note the units of mag arcsec^{-2}). We normalize the values radially by r_{bar} and r_d returned by GALFIT. For simplicity in this comparison, we exclude sample galaxies modelled by S15 using two disks.

There is good agreement between the disks recovered by DISKFIT and GALFIT for $r > 2r_d$ in Figure 11a), although DISKFIT attributes slightly more light to the disk as r increases. For $r < 1.5r_d$ in the sample as a whole, there is more light in the exponential GALFIT disks than their non-parametric DISKFIT counterparts; this is also the case in the individual models shown in Figures 7–9. Figure 11b) shows that this light is being attributed to the bar, which has a higher surface brightness for $0 < r < r_{bar}$ in the DISKFIT models compared to the GALFIT models. A larger $\Delta\mu$ is found for $r > 0.8r_{bar}$, where the non-parametric DISKFIT bars are several times brighter than the Ferrers GALFIT bars (albeit in a region where the bar itself is faint). We note that this behaviour is not seen in the fits to simulated galaxies (c.f. Figure 6), where DISKFIT cleanly recovers true exponential disks and Ferrers bars. This suggests that the surface brightness distributions in the S⁴G galaxies are more complicated than the sum of these two components.

We note that cumulative properties derived from photometric fits are even more uncertain. Figure 12 compares the light fractions implied by our DISKFIT and the S15 GALFIT fits for comparison sample galaxies that include both components: unless the fraction of light in the disk exceeds $\simeq 85\%$, the relative brightnesses of the disk and bar components can differ by over 30%.

5 DISCUSSION AND CONCLUSIONS

We have presented non-parametric photometric models of over 500 disk galaxies from S⁴G using DISKFIT. We use a suite of simulated galaxies embedded in S⁴G-like images to validate DISKFIT’s performance on our 570-galaxy S⁴G subsample (§3.2, Figures 2 and 3), and find that DISKFIT non-parametrically recovers the geometry and surface brightness distributions of exponential disks and Ferrers bars as long as their position angles differ by more than 5° (Figures 5 and 6). By contrast, DISKFIT does not reliably recover the Sérsic bulge properties of our simulated galaxies (Figure 4) and we ignore the bulge region in our subsequent S⁴G fits.

We then carry out DISKFIT decompositions of the 532 S⁴G subsample galaxies with $|\text{PA}_{\text{disk}} - \text{PA}_{\text{bar}}| > 5^\circ$ as deter-

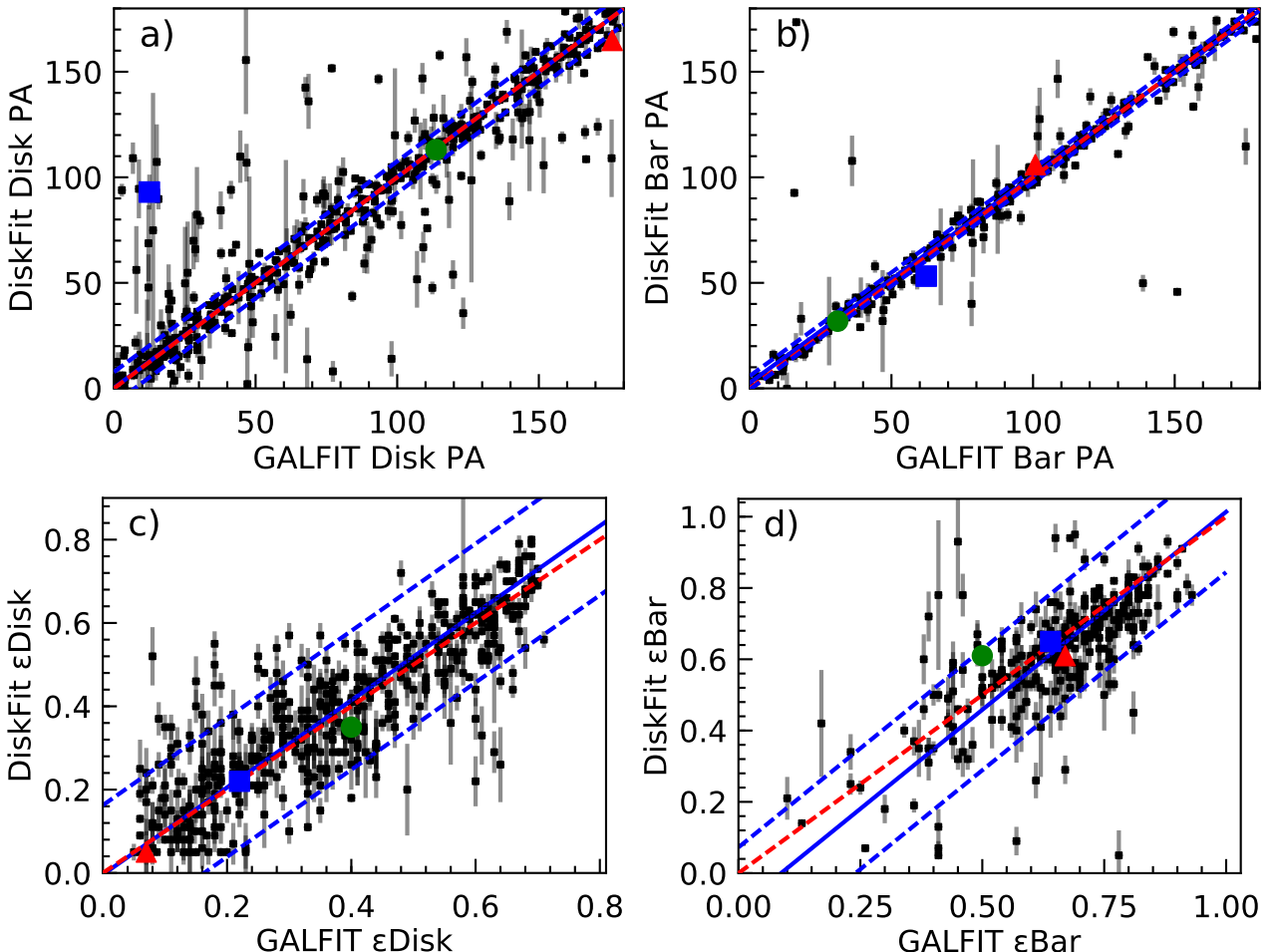


Figure 10. The position angle recovered by DISKFIT for **a**): the disk as a function of the values adopted in the GALFIT models and **b**): the bar as a function of that recovered by GALFIT, and the ellipticity recovered by DISKFIT for **c**): the disk and **d**): the bar as a function of that recovered by GALFIT. The dashed red line is the 1:1 relation, solid blue is the best-fitting linear least squares relationship, and the dashed blue lines show two times the normalized median absolute deviation (MAD/1.4826) about the best fit. The coloured points indicate the comparison sample galaxies shown in Figures 7 to 9.

mined by S15 and adopted by the parametric GALFIT algorithm (Table 1), and compare the best-fitting parameters to the S15 values. While on the whole the DISKFIT and GALFIT models return similar results, we find that discrepancies between the best-fitting disk and bar geometries of some systems well exceed the uncertainties that we estimate using a robust bootstrap resampling technique. Comparing the disk and bar surface brightness profiles, we find that DISKFIT attributes more light to the bar and less to the disk than in the S15 GALFIT models across the extent of the bar (Figure 11). This difference is particularly striking for $r \gtrsim 0.8r_{bar}$, where the non-parametric DISKFIT bars are several times brighter than the Ferrers GALFIT bars.

The failure of DISKFIT to recover bulges in simulated S⁴G-like images highlights the importance of validating decomposition algorithms, especially before applying them to large samples of real systems (e.g. Schombert & Bothun 1987; Byun & Freeman 1995; Wadadekar et al. 1999; MacArthur et al. 2003; Gadotti 2008; Peters & Kuzio de Naray 2017). It is possible that the non-parametric nature of DISKFIT makes bulge recovery more difficult than

for parametric algorithms such as GALFIT, though Gadotti (2008) finds that bulges with r_{eff} comparable to the seeing radius are difficult to recover even when both the bulge and the disk are parametrized. We caution against the adoption of bulge parameters derived from 2D decompositions that do not include quantitative estimates of the associated uncertainties and algorithms limitations through simulations (e.g. S15, Wadadekar et al. 1999; Janz et al. 2014; Bittner et al. 2017).

The relatively large scatter between the best-fitting DISKFIT parameters and those adopted in the S15 models in our S⁴G comparison subsample suggests that, unless the (unreported) uncertainties in the S15 GALFIT fits are considerably larger than those that we derive using DISKFIT for the majority of the sample, different photometric decomposition approaches can return significantly different structural properties for disks and bars in nearby galaxies (e.g. Byun & Freeman 1995; Peng et al. 2010). For S⁴G disk galaxies in particular, our DISKFIT and GALFIT comparisons suggest that their disk and bar ellipticities are typically constrained

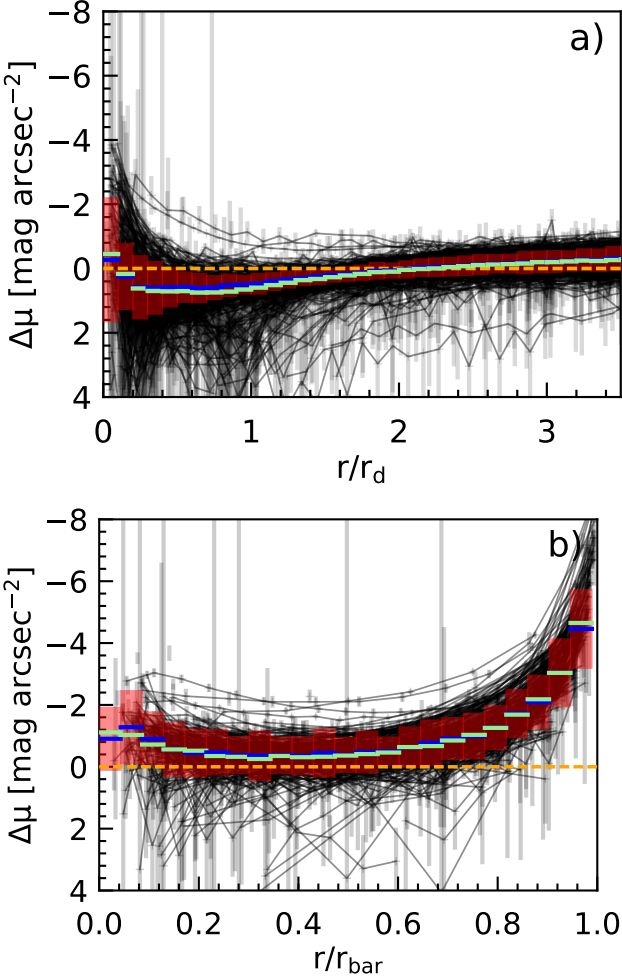


Figure 11. The difference between the surface brightness measured by DISKFIT and the GALFIT profiles for **a)**: bar surface brightness profiles (Ferrers bars), and **b)**: disk surface brightness profiles (exponential disks). The dashed yellow line indicates the point where the difference is zero. The red bars show the interquartile range, with the blue horizontal lines indicating the median within each bar and light green showing the mean within each bar. Note that the range of y-values in these figures are approximately twice that of Figure 6, and that the values for r_{bar} and r_d are those recovered by S15 using GALFIT. In this plot we exclude the galaxies fit by two disks in S15.

to no better than $\Delta\epsilon \sim 0.1$ on average, while much larger uncertainties are implied by the outliers in Figure 10.

Our DISKFIT models of the S⁴G comparison sample were constrained to have the same number of components and initial conditions as those reported by S15 using GALFIT. While a detailed investigation of the impact of structural component and initial guess selection on model uncertainties is beyond the scope of this paper, we speculate that these effects would further widen the gap between parameters derived using different photometric modelling techniques. As explained in §4.1, there are some sample galaxies for which DISKFIT failed to converge on even a disk-only model when initiated using the best fitting values from S15 as inputs. We suspect that this stems from the susceptibility

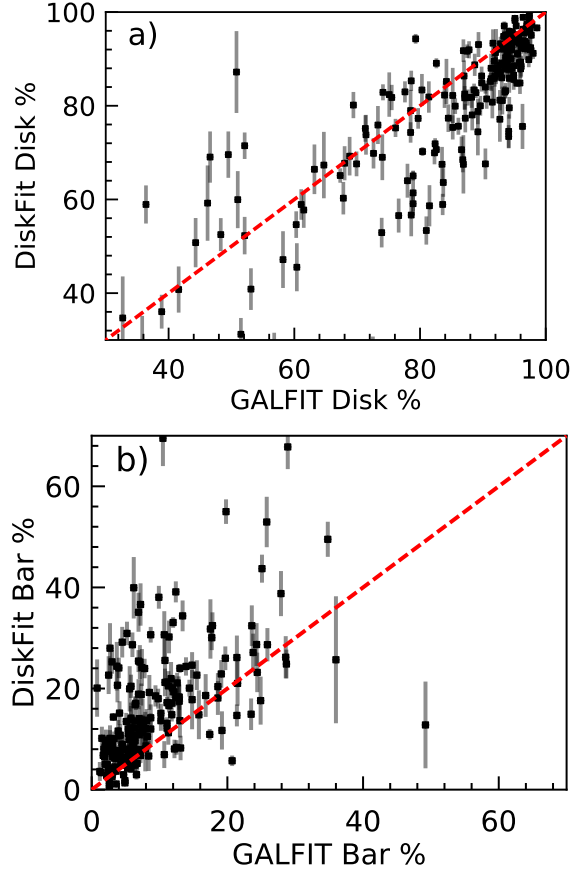


Figure 12. The fraction of light recovered within **a)**: the disk and **b)**: the bar by DISKFIT as a function of that recovered by GALFIT. The dashed red line is 1:1 relation.

Parameter (Figure 5)	α (1)	β (2)	MAD (3)
ϵ_{Disk}	1.000(0.007)	-0.003(0.003)	0.0043
ϵ_{Bar}	0.965(0.008)	0.025(0.005)	0.014
Disk PA (°)	1.0000(0.0001)	-0.009(0.004)	0.25
Bar PA (°)	1.0000(0.0001)	-0.018(0.003)	0.36

Parameter (Figure 10)	α	β	MAD
ϵ_{Disk}	1.05(0.02)	-0.01 (0.01)	0.083
ϵ_{Bar}	1.11(0.03)	-0.10 (0.02)	0.085
Disk PA (°)	0.998(0.003)	0.2 (0.2)	7.5
Bar PA (°)	0.98(0.01)	3 (1)	3.2

Table 2. Best-fitting linear least squares regression parameters for relations shown in Figure 5 (synthetic sample) and in Figure 10 (S⁴G subsample). Column 1: parameter of interest. Columns 2 and 3: best-fitting slope (α) and intercept (β) from a linear least-squares fit $P_{DF} = \alpha P_x + \beta$, where P_{DF} is the best-fitting DISKFIT value and P_x is the true value in the Figure 5 trends, and the value adopted by GALFIT in S15 in the Figure 10 trends (numbers in parentheses are the uncertainties on the reported values). Column 4: median absolute deviation of the best-fitting DISKFIT values.

of the Levenberg-Marquardt minimization scheme adopted by DISKFIT and GALFIT to local minima in the χ^2 landscape. Indeed, recent kinematic model tests by Bekiaris et al. (2016) show that the optimization method itself may also affect the best-fitting values obtained from the same modelling algorithm. We therefore conclude that the differences we find between the DISKFIT and GALFIT fits to the comparison sample galaxies likely underestimate the true uncertainties in S^4G disk galaxy structural parameters recovered from 2D decomposition algorithms.

In light of our simulations demonstrating that DISKFIT accurately disentangles exponential disks from Ferrers bars, the differences between the surface brightness profiles recovered by DISKFIT and the S15 GALFIT models implies that the surface brightness distributions of the S^4G comparison sample are not well-represented by these functional forms. The deficit of disk light that we find in the bar region is reminiscent of the ' Θ ' shaped features recovered in some decompositions of real galaxies (e.g. Laurikainen et al. 2005; Gadotti 2008; Kim et al. 2016a), as well as in simulations (e.g. Athanassoula & Misiriotis 2002). At the same time, the excess of bar light recovered by DISKFIT relative to the S15 GALFIT fits, particularly for $r > 0.8r_{bar}$, implies that we non-parametrically recover brighter, longer bars than found in comparable Ferrers fits. We therefore concur with Williams & Evans (2017) that real galactic bars may exhibit important differences from the Ferrers function form. This is particularly relevant when a bar's length is used as a proxy for its evolutionary state (Hoyle et al. 2011; Aguerri et al. 2015; Carles et al. 2016). It is possible that bar lengths derived from non-parametric 2D models such as DISKFIT better represent their evolutionary states than do their Ferrers r_{bar} , but a careful validation of this hypothesis using mock and simulated galaxies is required (e.g. Athanassoula & Misiriotis 2002; Aguerri et al. 2009). We defer such an exploration using DISKFIT to future work.

ACKNOWLEDGEMENTS

Computations were performed on resources and with support provided by the Centre for Advanced Computing (CAC) at Queen's University in Kingston, Ontario. The CAC is funded by: the Canada Foundation for Innovation, the Government of Ontario, and Queen's University. KS acknowledges support from the Natural Sciences and Engineering Research Council of Canada (NSERC).

REFERENCES

- Aguerri J. A. L., Méndez-Abreu J., Corsini E. M., 2009, *A&A*, **495**, 491
- Aguerri J. A. L., et al., 2015, *A&A*, **576**, A102
- Athanassoula E., 1992, *MNRAS*, **259**, 328
- Athanassoula E., 2002, *ApJ*, **569**, L83
- Athanassoula E., 2003, *MNRAS*, **341**, 1179
- Athanassoula E., 2013, Bars and secular evolution in disk galaxies: Theoretical input. p. 305
- Athanassoula E., Misiriotis A., 2002, *MNRAS*, **330**, 35
- Athanassoula E., Machado R. E. G., Rodionov S. A., 2013, *MNRAS*, **429**, 1949
- Bekiaris G., Glazebrook K., Fluke C. J., Abraham R., 2016, *MNRAS*, **455**, 754
- Binney J., Tremaine S., 1987, Galactic dynamics
- Bittner A., Gadotti D. A., Elmegreen B. G., Athanassoula E., Elmegreen D. M., Bosma A., Muñoz-Mateos J.-C., 2017, *MNRAS*, **471**, 1070
- Blanton M. R., et al., 2005, *AJ*, **129**, 2562
- Burstein D., 1979, *ApJ*, **234**, 435
- Byun Y. I., Freeman K. C., 1995, *ApJ*, **448**, 563
- Capaccioli M., 1989, in Corwin Jr. H. G., Bottinelli L., eds, *World of Galaxies (Le Monde des Galaxies)*. pp 208–227
- Carles C., Martel H., Ellison S. L., Kawata D., 2016, *MNRAS*, **463**, 1074
- Englmaier P., Gerhard O., 1997, *MNRAS*, **287**, 57
- Erroz-Ferrer S., et al., 2015, *MNRAS*, **451**, 1004
- Erwin P., 2005, *MNRAS*, **364**, 283
- Erwin P., 2015, *ApJ*, **799**, 226
- Ferrers N. M., 1877, *Quart. J. Pure and Appl. Math.*, **14**, 1
- Gadotti D. A., 2008, *MNRAS*, **384**, 420
- Hohl F., 1971, *ApJ*, **168**, 343
- Holmes L., et al., 2015, *MNRAS*, **451**, 4397
- Hoyle B., et al., 2011, *MNRAS*, **415**, 3627
- Janz J., et al., 2014, *ApJ*, **786**, 105
- Kent S. M., 1985, *ApJS*, **59**, 115
- Kim K., Oh S., Jeong H., Aragón-Salamanca A., Smith R., Yi S. K., 2016a, *ApJS*, **225**, 6
- Kim T., Gadotti D. A., Athanassoula E., Bosma A., Sheth K., Lee M. G., 2016b, *MNRAS*, **462**, 3430
- Kormendy J., 1977a, *ApJ*, **214**, 359
- Kormendy J., 1977b, *ApJ*, **217**, 406
- Kormendy J., 1977c, *ApJ*, **218**, 333
- Kormendy J., 2013, Secular Evolution in Disk Galaxies. p. 1
- Kormendy J., Kennicutt Jr. R. C., 2004, *ARA&A*, **42**, 603
- Kruk S. J., et al., 2018, *MNRAS*, **473**, 4731
- Kuzio de Naray R., Arsenault C. A., Spekkens K., Sellwood J. A., McDonald M., Simon J. D., Teuben P., 2012, *MNRAS*, **427**, 2523
- Laurikainen E., Salo H., Buta R., 2005, *MNRAS*, **362**, 1319
- Ma C., de Grijs R., Ho L. C., 2017, *ApJS*, **230**, 14
- MacArthur L. A., Courteau S., Holtzman J. A., 2003, *ApJ*, **582**, 689
- Marleau F. R., Simard L., 1998, *ApJ*, **507**, 585
- Masters K. L., et al., 2011, *MNRAS*, **411**, 2026
- Muñoz-Mateos J. C., et al., 2013, *ApJ*, **771**, 59
- Muñoz-Mateos J. C., et al., 2015, *ApJS*, **219**, 3
- Mutlu Pakdil B., Mangedarage M., Seigar M. S., Treuthardt P., 2017, *MNRAS*, **466**, 355
- Peng C. Y., Ho L. C., Impey C. D., Rix H.-W., 2002, *AJ*, **124**, 266
- Peng C. Y., Ho L. C., Impey C. D., Rix H.-W., 2010, *AJ*, **139**, 2097
- Pérez I., et al., 2017, *MNRAS*, **470**, L122
- Peters W., Kuzio de Naray R., 2017, *MNRAS*, **469**, 3541
- Querejeta M., et al., 2015, *ApJS*, **219**, 5
- Randriamampandry T. H., Deg N., Carignan C., Combes F., Spekkens K., 2016, *A&A*, **594**, A86
- Salo H., et al., 2015, *ApJS*, **219**, 4
- Schombert J. M., Bothun G. D., 1987, *AJ*, **93**, 60
- Sellwood J. A., 1981, *A&A*, **99**, 362
- Sellwood J. A., 2013, Dynamics of Disks and Warps. p. 923, doi:10.1007/978-94-007-5612-0_18
- Sellwood J. A., 2014, *Reviews of Modern Physics*, **86**, 1
- Sellwood J. A., Sánchez R. Z., 2010, *MNRAS*, **404**, 1733
- Sellwood J. A., Spekkens K., 2015, preprint, ([arXiv:1509.07120](https://arxiv.org/abs/1509.07120))
- Sérsic J. L., 1963, Boletín de la Asociación Argentina de Astronomía La Plata Argentina, **6**, 41
- Sheth K., et al., 2010, *PASP*, **122**, 1397
- Simard L., et al., 2002, *ApJS*, **142**, 1
- Sorce J. G., Creasey P., Libeskind N. I., 2016, *MNRAS*, **455**, 2644
- Spekkens K., Sellwood J. A., 2007, *ApJ*, **664**, 204

- Tonini C., Mutch S. J., Croton D. J., Wyithe J. S. B., 2016, *Monthly Notices of the Royal Astronomical Society*, 459, 4109
Vika M., Bamford S. P., Häubler B., Rojas A. L., Borch A., Nichol R. C., 2013, *MNRAS*, 435, 623
Wadadekar Y., Robbason B., Kembhavi A., 1999, *AJ*, 117, 1219
Weinzirl T., Jogee S., Barazza F. D., 2008, in Frebel A., Maund J. R., Shen J., Siegel M. H., eds, Astronomical Society of the Pacific Conference Series Vol. 393, New Horizons in Astronomy. p. 279 ([arXiv:0802.3903](https://arxiv.org/abs/0802.3903))
Williams A. A., Evans N. W., 2017, *MNRAS*, 469, 4414
Wozniak H., Friedli D., Martinet L., Martin P., Bratschi P., 1995, *A&AS*, 111, 115
de Souza R. E., Gadotti D. A., dos Anjos S., 2004, *ApJS*, 153, 411
de Swardt B., et al., 2015, *ApJ*, 808, 90

APPENDIX A: FULL TABLE 1

Name (1)	Model (2)	Disk PA [°] (3)	ϵ_{Disk} (4)	Bar PA [°] (5)	ϵ_{Bar} (6)	Disk % (7)	Bar % (8)	flags (9)
ESO012-010	dbar	151(1)	0.62(0.02)	24(3)	0.44(0.04)	88(1)	12(1)	
ESO013-016	dbar	N/A	N/A	N/A	N/A	N/A	N/A	a
ESO026-001	dbar	45(14)	0.25(0.07)	71(1)	0.77(0.02)	92(1)	7.6(1.3)	b
ESO027-001	bdbar	93(8)	0.22(0.06)	53(2)	0.65(0.05)	82(3)	12(3)	
ESO027-008	d	145(2)	0.64(0.02)	N/A	N/A	N/A	N/A	b
ESO048-017	dbar	N/A	N/A	N/A	N/A	N/A	N/A	a b
ESO054-021	dbar	82(1)	0.50(0.03)	41(9)	0.37(0.04)	93(2)	7.4(2.0)	
ESO079-005	dbar	183(2)	0.53(0.03)	13(1)	0.76(0.02)	74(4)	26(4)	
ESO120-012	d	94(3)	0.51(0.04)	N/A	N/A	N/A	N/A	c
ESO150-005	d	48(16)	0.09(0.04)	N/A	N/A	N/A	N/A	c
ESO285-048	dbar	81(1)	0.59(0.02)	96(1)	0.78(0.03)	92(1)	7.5(1.0)	
ESO289-048	dbar	141(1)	0.71(0.02)	164(9)	0.50(0.06)	92(2)	8.4(2.4)	
ESO298-015	dbar	61(1)	0.63(0.01)	39(3)	0.67(0.04)	93(1)	7.5(1.4)	
ESO342-013	dbar	158(2)	0.69(0.03)	155(1)	0.93(0.02)	82(5)	18(5)	
ESO342-050	bd	36(3)	0.39(0.04)	N/A	N/A	95(1)	N/A	
ESO345-046	dbar	91(8)	0.15(0.03)	113(2)	0.58(0.03)	92(1)	7.6(1.5)	
ESO347-029	dbar	118(24)	0.26(0.09)	90(26)	0.93(0.16)	96(2)	3.8(1.8)	b
ESO357-012	dbar	129(2)	0.29(0.01)	104(3)	0.55(0.04)	86(3)	14(3)	
ESO359-003	d	128(1)	0.73(0.01)	N/A	N/A	N/A	N/A	c
ESO400-025	dbar	N/A	N/A	N/A	N/A	N/A	N/A	a
ESO402-026	bdbar	106(1)	0.46(0.02)	80(4)	0.36(0.05)	59(4)	32(4)	
ESO404-017	d	122(1)	0.60(0.02)	N/A	N/A	N/A	N/A	c
ESO404-027	dbar	N/A	N/A	N/A	N/A	N/A	N/A	a b
ESO407-009	d	31(2)	0.59(0.03)	N/A	N/A	N/A	N/A	b
ESO423-002	dbar	N/A	N/A	N/A	N/A	N/A	N/A	a
ESO440-004	dbar	85(3)	0.53(0.06)	124(2)	0.52(0.01)	82(3)	18(3)	
ESO443-069	dbar	157(9)	0.14(0.04)	177(1)	0.75(0.02)	91(1)	9.2(1.2)	
ESO444-037	d	124(2)	0.46(0.04)	N/A	N/A	N/A	N/A	b
ESO445-089	dbar	108(8)	0.23(0.05)	137(4)	0.56(0.06)	94(2)	6.0(1.6)	b
ESO481-018	dbar	N/A	N/A	N/A	N/A	N/A	N/A	a b
ESO482-035	dbar	5.7(1.2)	0.38(0.01)	30(1)	0.71(0.01)	83(1)	17(1)	
ESO504-028	d	14(15)	0.08(0.03)	N/A	N/A	N/A	N/A	b
ESO505-009	d	78(1)	0.62(0.02)	N/A	N/A	N/A	N/A	
ESO508-024	dbar	73(8)	0.40(0.04)	51(3)	0.71(0.05)	98(1)	2(1)	
ESO508-051	d	53(2)	0.44(0.03)	N/A	N/A	N/A	N/A	
ESO510-059	dbar	103(7)	0.38(0.08)	115(1)	0.77(0.01)	85(2)	15(2)	
ESO532-022	dbar	119(4)	0.50(0.04)	27(3)	0.57(0.06)	85(2)	15(2)	
ESO541-004	bd	26(1)	0.54(0.01)	N/A	N/A	97(1)	N/A	
ESO544-030	d	108(2)	0.28(0.02)	N/A	N/A	N/A	N/A	c
ESO548-025	dbar	85(4)	0.41(0.08)	168(1)	0.54(0.03)	82(6)	18(6)	
ESO549-018	bd	20(2)	0.47(0.02)	N/A	N/A	99(1)	N/A	
ESO550-024	d	124(2)	0.55(0.03)	N/A	N/A	N/A	N/A	c
ESO576-003	bd	95(1)	0.64(0.03)	N/A	N/A	79(2)	N/A	
ESO576-017	dbar	115(9)	0.11(0.04)	5.8(2.9)	0.95(0.04)	99(1)	1(1)	b
ESO576-032	dbar	151(3)	0.32(0.03)	153(1)	0.80(0.03)	96(1)	4(1)	b
ESO580-022	dbar	156(3)	0.32(0.04)	129(3)	0.69(0.05)	93(2)	6.6(1.8)	
IC0163	dbar	84(1)	0.55(0.02)	71(2)	0.77(0.03)	86(2)	14(2)	
IC0167	dbar	59(5)	0.30(0.05)	122(4)	0.56(0.04)	91(1)	9.2(1.4)	c
IC0529	dbar	147(3)	0.51(0.04)	145(2)	0.61(0.01)	92(2)	7.7(2.0)	b
IC0600	dbar	-2(1)	0.49(0.03)	204(4)	0.24(0.02)	55(5)	45(5)	c
IC0749	dbar	158(3)	0.28(0.02)	42(2)	0.63(0.04)	96(1)	4(1)	b
IC0758	dbar	15(11)	0.19(0.05)	52(1)	0.71(0.03)	89(2)	11(2)	
IC0769	dbar	34(2)	0.49(0.03)	16(2)	0.72(0.03)	97(1)	3(1)	b
IC0776	d	67(12)	0.29(0.11)	N/A	N/A	N/A	N/A	c
IC0800	dbar	151(3)	0.40(0.03)	151(2)	0.76(0.01)	88(2)	12(2)	
IC1067	bdbar	123(4)	0.22(0.03)	151(1)	0.65(0.03)	80(3)	18(3)	b
IC1151	dbar	36(1)	0.52(0.02)	36(2)	0.75(0.06)	94(2)	6.1(2.0)	
IC1158	d	136(2)	0.47(0.02)	N/A	N/A	N/A	N/A	b

Name (1)	Model (2)	Disk PA [°] (3)	ϵ Disk (4)	Bar PA [°] (5)	ϵ Bar (6)	Disk % (7)	Bar % (8)	flags (9)
IC1438	bdbar	149(2)	0.08(0.01)	123(1)	0.59(0.04)	71(3)	23(3)	
IC1532	dbar	74(1)	0.67(0.02)	74(2)	0.75(0.03)	92(4)	8.1(4.4)	
IC1892	dbar	16(7)	0.41(0.08)	19(1)	0.81(0.01)	92(1)	7.9(1.3)	
IC1914	dbar	104(3)	0.46(0.04)	97(3)	0.50(0.03)	83(4)	17(4)	b
IC1933	dbar	56(2)	0.45(0.02)	48(2)	0.68(0.08)	94(2)	6.3(2.0)	
IC1953	bdbar	121(4)	0.22(0.02)	153(1)	0.55(0.01)	85(1)	14(1)	
IC1954	dbar	66(10)	0.31(0.08)	95(1)	0.74(0.01)	97(1)	3(1)	
IC2627	bd	N/A	N/A	N/A	N/A	N/A	N/A	f
IC3115	dbar	-14(13)	0.23(0.08)	155(3)	0.69(0.06)	97(1)	3.1(1.5)	
IC3391	d	67(3)	0.34(0.02)	N/A	N/A	N/A	N/A	b
IC3806	d	179(1)	~ 0.66	N/A	N/A	N/A	N/A	c
IC3881	dbar	24(1)	0.66(0.01)	16(2)	0.81(0.04)	93(3)	6.9(2.7)	
IC4216	bd	~ 50	~ 0.53	N/A	N/A	N/A	N/A	c d
IC4237	bdbar	138(2)	0.31(0.02)	118(1)	0.78(0.02)	93(1)	7(1)	
IC4536	dbar	-11(6)	0.16(0.03)	167(1)	0.73(0.01)	91(1)	9(1)	b
IC4901	dbar	N/A	N/A	N/A	N/A	N/A	N/A	a b c
IC4986	d	21(2)	0.51(0.02)	N/A	N/A	N/A	N/A	c
IC5039	bd	~ 160	~ 0.62	N/A	N/A	N/A	N/A	c d
IC5201	dbar	29(1)	0.61(0.02)	15(1)	0.71(0.01)	90(2)	9.7(1.5)	
IC5240	bdbar	102(2)	0.35(0.03)	88(1)	0.65(0.03)	47(6)	28(5)	
IC5269C	dbar	64(1)	0.65(0.03)	62(23)	0.78(0.21)	95(1)	4.8(1.2)	
IC5271	bd	137(1)	0.63(0.01)	N/A	N/A	89(1)	N/A	
IC5273	dbar	43(4)	0.48(0.04)	37(3)	0.88(0.02)	99(1)	1(1)	
NGC0115	d	121(1)	0.57(0.02)	N/A	N/A	N/A	N/A	c
NGC0150	bdbar	118(3)	0.46(0.06)	58(3)	0.32(0.03)	68(3)	24(2)	
NGC0157	bd	43(13)	0.35(0.13)	N/A	N/A	97(1)	N/A	
NGC0210	bdbar	175(2)	0.15(0.03)	172(1)	0.55(0.04)	70(5)	26(4)	
NGC0255	dbar	210(8)	0.15(0.03)	56(2)	0.73(0.03)	94(1)	6(1)	b
NGC0289	dbar	N/A	N/A	N/A	N/A	N/A	N/A	a b
NGC0337	dbar	124(4)	0.46(0.05)	174(2)	0.62(0.06)	74(5)	26(5)	
NGC0406	dbar	159(4)	0.57(0.06)	33(8)	0.49(0.06)	86(3)	14(3)	
NGC0450	dbar	75(8)	0.32(0.05)	21(3)	0.64(0.06)	96(1)	4(1)	
NGC0470	bd	153(2)	0.35(0.05)	N/A	N/A	91(2)	N/A	
NGC0514	bd	106(4)	0.30(0.03)	N/A	N/A	95(1)	N/A	
NGC0578	dbar	109(1)	0.54(0.02)	91(2)	0.60(0.04)	91(2)	9.3(1.9)	b
NGC0600	dbar	2(22)	0.06(0.04)	19(1)	0.78(0.01)	87(1)	13(1)	
NGC0615	bdbar	N/A	N/A	N/A	N/A	N/A	N/A	a
NGC0628	bd	~ 200	~ 0.05	N/A	N/A	~ 90	N/A	e
NGC0658	d	28(1)	0.44(0.01)	N/A	N/A	N/A	N/A	b c
NGC0672	dbar	71(1)	0.64(0.01)	78(1)	0.80(0.01)	80(2)	20(2)	
NGC0685	dbar	120(32)	0.06(0.06)	55(1)	0.68(0.02)	92(1)	7.7(1.2)	
NGC0718	bdbar	8.2(4.5)	~ 0.05	150(2)	0.53(0.04)	66(5)	19(3)	
NGC0755	dbar	N/A	N/A	N/A	N/A	N/A	N/A	a
NGC0772	bd	114(4)	0.25(0.04)	N/A	N/A	96(2)	N/A	c
NGC0779	bd	161(1)	0.70(0.01)	N/A	N/A	71(2)	N/A	
NGC0895	d	116(4)	0.37(0.04)	N/A	N/A	N/A	N/A	b c
NGC0918	bd	157(9)	0.30(0.07)	N/A	N/A	99(16)	N/A	
NGC0941	dbar	165(6)	0.23(0.05)	42(2)	0.65(0.04)	91(2)	9.3(1.9)	b
NGC0986	bdbar	N/A	N/A	N/A	N/A	N/A	N/A	f
NGC0991	dbar	89(13)	0.05(0.02)	82(2)	0.57(0.08)	97(1)	3(1)	b
NGC1015	bdbar	16(6)	0.11(0.02)	101(1)	0.71(0.02)	65(2)	17(1)	
NGC1022	bdbar	165(3)	0.05(0.08)	106(3)	0.61(0.06)	67(7)	13(5)	
NGC1042	bd	109(7)	0.26(0.05)	N/A	N/A	98(1)	N/A	b
NGC1073	dbar	11(31)	0.06(0.05)	62(1)	0.73(0.01)	88(1)	12(1)	
NGC1076	d	100(1)	0.48(0.01)	N/A	N/A	N/A	N/A	b c
NGC1079	bdbar	89(3)	0.34(0.03)	111(2)	0.40(0.02)	44(3)	41(3)	b
NGC1084	bd	41(2)	0.40(0.03)	N/A	N/A	87(3)	N/A	
NGC1087	dbar	4(13)	0.25(0.08)	125(1)	0.66(0.01)	94(1)	6(1)	
NGC1090	bd	105(2)	0.53(0.06)	N/A	N/A	95(15)	N/A	
NGC1097	dbar	145(3)	0.11(0.01)	145(1)	0.61(0.03)	68(3)	32(3)	c

Name (1)	Model (2)	Disk PA [°] (3)	ϵ Disk (4)	Bar PA [°] (5)	ϵ Bar (6)	Disk % (7)	Bar % (8)	flags (9)
NGC1179	dbar	31(7)	0.24(0.05)	154(2)	0.64(0.02)	97(1)	3(1)	b
NGC1187	bdbar	N/A	N/A	N/A	N/A	N/A	N/A	a
NGC1232	bdbar	78(2)	~ 0.05	102(5)	0.26(0.05)	88(2)	8.0(2.1)	
NGC1249	dbar	84(1)	0.62(0.02)	76(1)	0.84(0.01)	82(3)	18(3)	b
NGC1255	dbar	118(3)	0.47(0.04)	120(2)	0.94(0.04)	100(1)	0.33(0.13)	
NGC1291	bdbar	N/A	N/A	N/A	N/A	N/A	N/A	f
NGC1292	bd	11(1)	0.57(0.01)	N/A	N/A	98(1)	N/A	
NGC1300	bdbar	101(3)	0.21(0.03)	102(2)	0.62(0.03)	71(3)	29(2)	
NGC1310	dbar	98(7)	0.17(0.03)	95(2)	0.88(0.02)	98(1)	2(1)	b
NGC1313	dbar	215(27)	0.11(0.04)	16(2)	0.52(0.06)	83(3)	17(3)	b e
NGC1325A	bd	-9(7)	0.11(0.03)	N/A	N/A	100(1)	N/A	e
NGC1350	bdbar	9.8(4.2)	0.31(0.04)	27(2)	0.50(0.02)	64(5)	34(4)	b e
NGC1357	bd	81(2)	0.24(0.03)	N/A	N/A	76(9)	N/A	c
NGC1367	bdbar	139(3)	0.29(0.03)	105(2)	0.51(0.04)	83(3)	14(3)	
NGC1398	bdbar	95(2)	0.27(0.03)	12(2)	0.59(0.03)	80(3)	13(1)	
NGC1436	bd	145(4)	0.37(0.03)	N/A	N/A	96(1)	N/A	c
NGC1452	bdbar	113(4)	0.35(0.02)	32(1)	0.61(0.02)	55(3)	26(2)	
NGC1476	dbar	N/A	N/A	N/A	N/A	N/A	N/A	a
NGC1483	dbar	136(4)	0.29(0.03)	3.4(1.5)	0.72(0.04)	86(3)	14(3)	
NGC1493	dbar	N/A	N/A	N/A	N/A	N/A	N/A	b f
NGC1494	dbar	N/A	N/A	N/A	N/A	N/A	N/A	a
NGC1511	dbar	N/A	N/A	N/A	N/A	N/A	N/A	a
NGC1512	bdbar	60(2)	0.24(0.03)	47(1)	0.51(0.01)	53(3)	38(2)	
NGC1519	dbar	107(1)	0.75(0.01)	90(3)	0.81(0.03)	89(2)	11(2)	
NGC1532	bd	35(1)	0.80(0.01)	N/A	N/A	81(1)	N/A	
NGC1559	dbar	N/A	N/A	N/A	N/A	N/A	N/A	f
NGC1566	dbar	~ 120	~ 0.29	~ 10	~ 0.58	~ 80	~ 20	b c e
NGC1672	bdbar	N/A	N/A	N/A	N/A	N/A	N/A	f
NGC1688	dbar	-18(4)	0.43(0.06)	134(1)	0.78(0.01)	76(2)	24(2)	b
NGC1744	dbar	174(1)	0.57(0.02)	175(1)	0.91(0.02)	94(1)	6.0(1.2)	b
NGC1792	bd	137(1)	0.59(0.02)	N/A	N/A	96(1)	N/A	
NGC1853	d	47(1)	0.70(0.01)	N/A	N/A	N/A	N/A	b
NGC1892	dbar	76(1)	0.73(0.01)	108(5)	0.56(0.03)	90(2)	9.5(1.7)	b
NGC2500	dbar	71(6)	0.13(0.03)	8.1(4.3)	0.41(0.14)	91(3)	9.2(2.9)	b
NGC2541	d	169(1)	0.51(0.01)	N/A	N/A	N/A	N/A	c
NGC2543	bdbar	35(2)	0.37(0.05)	81(3)	0.35(0.03)	57(4)	25(2)	
NGC2604	dbar	156(26)	0.08(0.05)	52(1)	0.69(0.02)	83(2)	17(2)	
NGC2608	dbar	64(3)	0.39(0.03)	82(4)	0.58(0.07)	76(8)	24(8)	b
NGC2633	bdbar	0(5)	0.33(0.08)	174(1)	0.79(0.04)	51(5)	12(4)	
NGC2648	bd	151(1)	0.56(0.02)	N/A	N/A	68(2)	N/A	c
NGC2655	bdbar	84(1)	0.09(0.01)	85(1)	0.32(0.03)	41(5)	40(6)	
NGC2701	dbar	30(8)	0.40(0.07)	32(21)	0.46(0.12)	97(1)	3(1)	
NGC2710	dbar	N/A	N/A	N/A	N/A	N/A	N/A	a b
NGC2712	bd	187(3)	0.40(0.06)	N/A	N/A	98(1)	N/A	
NGC2715	bd	16(2)	0.52(0.03)	N/A	N/A	94(2)	N/A	
NGC2742	d	86(1)	0.51(0.01)	N/A	N/A	N/A	N/A	b
NGC2750	bdbar	84(3)	0.35(0.03)	52(5)	0.43(0.08)	77(2)	7.2(2.1)	
NGC2775	bd	158(1)	0.21(0.01)	N/A	N/A	79(1)	N/A	c
NGC2805	d	89(9)	0.17(0.04)	N/A	N/A	N/A	N/A	b c
NGC2844	d	10(1)	0.51(0.01)	N/A	N/A	N/A	N/A	b c
NGC2903	bdbar	~ 10	~ 0.51	~ 30	~ 0.71	~ 80	~ 20	e
NGC2964	bd	99(5)	0.26(0.06)	N/A	N/A	93(3)	N/A	
NGC2966	bdbar	68(1)	0.25(0.07)	76(1)	0.61(0.01)	41(4)	39(2)	
NGC2967	d	N/A	N/A	N/A	N/A	N/A	N/A	b f
NGC2968	bdbar	77(4)	0.24(0.03)	43(2)	0.48(0.05)	59(8)	32(6)	
NGC2976	dbar	N/A	N/A	N/A	N/A	N/A	N/A	a
NGC2985	bd	178(1)	0.19(0.01)	N/A	N/A	94(1)	N/A	c
NGC3020	dbar	N/A	N/A	N/A	N/A	N/A	N/A	a
NGC3027	dbar	130(2)	0.64(0.02)	119(2)	0.71(0.01)	92(2)	7.8(1.8)	
NGC3031	bd	149(2)	0.34(0.09)	N/A	N/A	100(11)	N/A	e

Name (1)	Model (2)	Disk PA [°] (3)	ϵ Disk (4)	Bar PA [°] (5)	ϵ Bar (6)	Disk % (7)	Bar % (8)	flags (9)
NGC3041	bd	97(2)	0.34(0.03)	N/A	N/A	96(2)	N/A	
NGC3057	dbar	4.6(4.1)	0.36(0.04)	172(1)	0.73(0.03)	91(1)	8.8(1.2)	
NGC3061	bdbar	190(6)	0.24(0.05)	157(2)	0.60(0.09)	93(2)	5.0(1.4)	
NGC3067	dbar	102(2)	0.62(0.02)	91(3)	0.67(0.05)	80(8)	20(8)	b
NGC3147	bd	106(13)	0.05(0.03)	N/A	N/A	91(6)	N/A	
NGC3153	dbar	163(1)	0.56(0.02)	180(1)	0.86(0.02)	93(1)	6.8(1.5)	
NGC3162	dbar	24(6)	0.30(0.04)	127(4)	0.67(0.04)	94(1)	6.2(1.2)	b
NGC3166	bdbar	87(1)	0.46(0.02)	167(5)	0.21(0.06)	69(5)	29(3)	
NGC3184	bd	N/A	N/A	N/A	N/A	N/A	N/A	b f
NGC3185	bd	128(2)	0.45(0.02)	N/A	N/A	82(4)	N/A	
NGC3198	bd	39(1)	0.74(0.03)	N/A	N/A	56(9)	N/A	
NGC3206	dbar	19(6)	0.33(0.04)	86(2)	0.52(0.03)	87(1)	13(1)	
NGC3246	dbar	94(2)	0.47(0.02)	85(2)	0.70(0.03)	95(1)	5.1(1.4)	
NGC3264	dbar	13(2)	0.60(0.04)	160(2)	0.71(0.03)	89(2)	11(2)	
NGC3287	dbar	17(1)	0.61(0.02)	14(1)	0.77(0.03)	76(5)	24(5)	
NGC3294	bd	117(2)	0.49(0.03)	N/A	N/A	99(1)	N/A	
NGC3310	d	233(7)	0.19(0.03)	N/A	N/A	N/A	N/A	b c
NGC3321	bd	33(5)	0.47(0.08)	N/A	N/A	93(5)	N/A	
NGC3346	dbar	128(11)	0.14(0.05)	90(1)	0.69(0.02)	97(1)	3(1)	
NGC3351	bdbar	12(1)	0.26(0.02)	112(2)	0.46(0.03)	82(3)	18(2)	
NGC3359	dbar	176(6)	0.41(0.06)	17(1)	0.77(0.01)	87(2)	13(2)	
NGC3361	d	155(1)	0.62(0.01)	N/A	N/A	N/A	N/A	b
NGC3380	bdbar	-160(2)	0.05(0.01)	20(1)	0.53(0.02)	41(5)	49(4)	b
NGC3381	dbar	24(11)	0.25(0.06)	79(2)	0.73(0.03)	79(3)	21(3)	
NGC3389	dbar	N/A	N/A	N/A	N/A	N/A	N/A	a
NGC3423	bd	39(6)	0.16(0.06)	N/A	N/A	99(8)	N/A	
NGC3430	bd	33(2)	0.49(0.02)	N/A	N/A	97(3)	N/A	
NGC3433	bd	188(5)	0.24(0.06)	N/A	N/A	96(4)	N/A	
NGC3440	bd	64(2)	0.55(0.19)	N/A	N/A	95(15)	N/A	
NGC3443	d	151(2)	0.44(0.02)	N/A	N/A	N/A	N/A	c
NGC3448	bd	63(1)	0.71(0.02)	N/A	N/A	74(11)	N/A	
NGC3485	bdbar	90(5)	0.19(0.02)	44(3)	0.53(0.03)	75(4)	23(4)	
NGC3486	bd	75(1)	0.21(0.02)	N/A	N/A	83(2)	N/A	c
NGC3511	dbar	77(1)	0.71(0.02)	68(3)	0.59(0.04)	88(3)	12(3)	
NGC3513	dbar	142(5)	0.25(0.03)	118(1)	0.70(0.03)	88(2)	12(2)	
NGC3521	bd	161(1)	0.48(0.01)	N/A	N/A	96(1)	N/A	c
NGC3549	d	36(1)	0.70(0.01)	N/A	N/A	N/A	N/A	b
NGC3589	d	51(1)	0.53(0.02)	N/A	N/A	N/A	N/A	
NGC3596	bd	108(18)	0.17(0.08)	N/A	N/A	94(6)	N/A	
NGC3611	bd	20(1)	0.25(0.02)	N/A	N/A	48(16)	N/A	
NGC3614	d	77(7)	0.23(0.05)	N/A	N/A	N/A	N/A	b
NGC3622	d	6(1)	0.47(0.01)	N/A	N/A	N/A	N/A	c
NGC3629	bd	34(4)	0.25(0.04)	N/A	N/A	99(9)	N/A	
NGC3631	bd	128(6)	0.10(0.03)	N/A	N/A	93(3)	N/A	
NGC3642	d	194(8)	0.18(0.03)	N/A	N/A	N/A	N/A	b c
NGC3652	dbar	150(9)	0.33(0.07)	170(1)	~0.91	92(2)	8.3(1.8)	b
NGC3655	d	N/A	N/A	N/A	N/A	N/A	N/A	b c f
NGC3666	bd	98(1)	0.73(0.01)	N/A	N/A	88(2)	N/A	
NGC3672	d	9(1)	0.61(0.01)	N/A	N/A	N/A	N/A	b
NGC3673	bdbar	77(1)	0.48(0.02)	82(1)	0.66(0.01)	65(3)	29(3)	b
NGC3675	d	0.49(0.98)	0.53(0.01)	N/A	N/A	N/A	N/A	b c
NGC3684	bdbar	124(2)	0.28(0.02)	136(2)	0.52(0.03)	86(5)	7.9(3.0)	
NGC3686	bdbar	18(3)	0.23(0.02)	84(3)	0.45(0.06)	89(2)	9.8(2.1)	
NGC3691	dbar	24(5)	0.28(0.04)	32(2)	0.72(0.07)	87(9)	13(9)	
NGC3705	bdbar	123(1)	0.56(0.01)	108(12)	0.13(0.05)	68(4)	24(4)	
NGC3726	bd	16(2)	0.43(0.03)	N/A	N/A	100(1)	N/A	
NGC3729	bdbar	163(1)	0.43(0.01)	28(2)	0.66(0.04)	84(1)	10(1)	
NGC3755	d	122(1)	0.53(0.02)	N/A	N/A	N/A	N/A	b c
NGC3756	bd	181(1)	0.52(0.01)	N/A	N/A	96(1)	N/A	
NGC3769	dbar	148(1)	0.68(0.01)	174(2)	0.66(0.02)	76(2)	24(2)	

Name (1)	Model (2)	Disk PA [°] (3)	ϵ Disk (4)	Bar PA [°] (5)	ϵ Bar (6)	Disk % (7)	Bar % (8)	flags (9)
NGC3780	bd	79(5)	0.25(0.04)	N/A	N/A	99(1)	N/A	
NGC3794	bd	119(2)	0.44(0.04)	N/A	N/A	81(9)	N/A	
NGC3795A	dbar	82(15)	0.11(0.04)	101(4)	0.31(0.05)	91(3)	9.0(2.9)	
NGC3810	bd	16(4)	0.30(0.04)	N/A	N/A	94(1)	N/A	c
NGC3813	d	83(1)	0.59(0.01)	N/A	N/A	N/A	N/A	b
NGC3850	dbar	123(1)	0.57(0.02)	113(2)	0.68(0.02)	81(3)	19(3)	
NGC3887	bdbar	13(2)	0.23(0.02)	177(1)	0.53(0.02)	73(2)	25(2)	
NGC3893	bd	-14(6)	0.29(0.09)	N/A	N/A	97(7)	N/A	
NGC3898	bd	107(1)	0.46(0.02)	N/A	N/A	81(4)	N/A	
NGC3901	bd	167(2)	0.55(0.02)	N/A	N/A	88(3)	N/A	
NGC3906	dbar	70(14)	0.11(0.03)	78(1)	0.76(0.01)	83(1)	17(1)	
NGC3913	bd	152(2)	~ 0.05	N/A	N/A	100(1)	N/A	c
NGC3930	bdbar	31(3)	0.35(0.05)	67(7)	0.49(0.06)	90(4)	9.8(2.9)	
NGC3938	bd	55(24)	0.05(0.03)	N/A	N/A	100(4)	N/A	
NGC3949	bd	121(2)	0.42(0.02)	N/A	N/A	100(1)	N/A	
NGC3953	bdbar	12(1)	0.52(0.01)	49(3)	0.55(0.04)	82(2)	11(2)	
NGC3956	dbar	59(1)	0.68(0.01)	60(2)	0.51(0.07)	90(2)	10(2)	
NGC3976	dbar	55(3)	0.54(0.05)	43(10)	0.35(0.08)	89(4)	11(4)	b
NGC3981	d	17(1)	0.61(0.02)	N/A	N/A	N/A	N/A	b
NGC3992	bdbar	~ 70	~ 0.42	~ 40	~ 0.6	~ 80	~ 10	b e
NGC4020	d	16(1)	0.65(0.01)	N/A	N/A	N/A	N/A	
NGC4027	dbar	-236(4)	0.36(0.04)	84(2)	0.61(0.03)	91(1)	9(1)	
NGC4034	dbar	11(1)	0.41(0.01)	62(3)	0.60(0.04)	95(1)	5(1)	b
NGC4037	dbar	194(2)	0.46(0.06)	-0(8)	0.05(0.07)	57(18)	43(18)	b
NGC4041	d	94(4)	0.21(0.02)	N/A	N/A	N/A	N/A	b c
NGC4045	bdbar	79(3)	0.23(0.06)	16(3)	0.46(0.03)	60(6)	23(4)	
NGC4050	bd	~ 80	~ 0.47	N/A	N/A	N/A	N/A	d
NGC4062	bd	99(1)	0.62(0.01)	N/A	N/A	95(1)	N/A	
NGC4064	dbar	159(2)	0.59(0.03)	167(1)	0.82(0.01)	85(2)	15(2)	
NGC4088	d	56(4)	0.54(0.05)	N/A	N/A	N/A	N/A	b
NGC4100	bd	163(1)	0.72(0.01)	N/A	N/A	91(1)	N/A	c
NGC4116	dbar	N/A	N/A	N/A	N/A	N/A	N/A	a
NGC4123	bdbar	125(3)	0.37(0.02)	106(1)	0.63(0.01)	59(2)	31(2)	
NGC4136	bdbar	110(12)	0.08(0.04)	19(7)	0.29(0.04)	92(2)	6.8(2.3)	
NGC4142	dbar	176(3)	0.42(0.03)	137(4)	0.68(0.03)	94(1)	6.3(1.4)	
NGC4145	dbar	84(5)	0.34(0.06)	136(3)	0.41(0.03)	95(1)	5(1)	
NGC4189	dbar	89(4)	0.34(0.03)	99(8)	0.40(0.09)	96(1)	4.3(1.2)	b
NGC4192	bd	152(1)	0.79(0.01)	N/A	N/A	81(1)	N/A	c
NGC4193	d	90(1)	0.53(0.02)	N/A	N/A	N/A	N/A	b
NGC4197	dbar	38(1)	0.79(0.02)	30(1)	0.87(0.02)	79(4)	21(4)	
NGC4212	bd	70(1)	0.46(0.02)	N/A	N/A	94(1)	N/A	
NGC4224	bd	56(3)	0.44(0.04)	N/A	N/A	97(1)	N/A	b
NGC4235	bd	49(1)	0.70(0.05)	N/A	N/A	63(9)	N/A	
NGC4242	d	18(4)	0.37(0.03)	N/A	N/A	N/A	N/A	
NGC4245	bdbar	-22(2)	0.20(0.01)	136(1)	0.53(0.02)	68(3)	20(2)	
NGC4254	bd	~ 70	~ 0.36	N/A	N/A	~ 90	N/A	c e
NGC4260	bdbar	60(2)	0.52(0.02)	39(3)	0.57(0.03)	57(5)	31(5)	
NGC4274	bdbar	100(1)	0.61(0.01)	93(2)	0.14(0.01)	65(1)	33(1)	
NGC4276	dbar	69(18)	0.11(0.04)	96(1)	0.75(0.04)	91(1)	8.6(1.3)	
NGC4286	d	153(2)	0.36(0.02)	N/A	N/A	N/A	N/A	b
NGC4288	dbar	169(6)	0.38(0.05)	9.9(2.5)	0.60(0.02)	81(3)	19(3)	
NGC4294	dbar	N/A	N/A	N/A	N/A	N/A	N/A	a
NGC4303	bd	~ 190	~ 0.2	N/A	N/A	~ 90	N/A	e
NGC4314	bdbar	~ 130	~ 0.17	~ 150	~ 0.73	~ 70	~ 30	b e
NGC4319	bdbar	136(7)	0.38(0.06)	163(2)	0.52(0.03)	76(4)	19(4)	
NGC4321	bd	119(3)	0.15(0.04)	N/A	N/A	98(1)	N/A	
NGC4351	dbar	60(1)	0.34(0.01)	88(2)	0.52(0.01)	95(1)	5(1)	c
NGC4378	bd	161(1)	0.20(0.01)	N/A	N/A	83(3)	N/A	c
NGC4380	bd	157(1)	~ 0.47	N/A	N/A	94(1)	N/A	
NGC4389	dbar	100(2)	0.51(0.03)	105(1)	0.84(0.01)	70(2)	30(2)	

Name (1)	Model (2)	Disk PA [°] (3)	ϵ Disk (4)	Bar PA [°] (5)	ϵ Bar (6)	Disk % (7)	Bar % (8)	flags (9)
NGC4390	dbar	98(2)	0.33(0.02)	120(2)	0.64(0.04)	97(1)	3(1)	b
NGC4393	d	19(2)	0.38(0.02)	N/A	N/A	N/A	N/A	
NGC4394	bdbar	120(7)	0.11(0.03)	145(1)	0.69(0.02)	83(2)	15(1)	
NGC4409	dbar	N/A	N/A	N/A	N/A	N/A	N/A	a c
NGC4411A	dbar	N/A	N/A	N/A	N/A	N/A	N/A	a
NGC4413	dbar	56(2)	0.33(0.02)	13(1)	0.62(0.02)	83(2)	17(2)	b
NGC4414	d	158(1)	0.41(0.01)	N/A	N/A	N/A	N/A	b
NGC4419	dbar	134(1)	0.67(0.02)	230(4)	0.59(0.05)	94(1)	6.2(1.3)	b
NGC4424	dbar	99(2)	0.56(0.02)	111(1)	0.79(0.01)	89(1)	11(1)	
NGC4430	dbar	92(8)	0.20(0.04)	120(3)	0.70(0.05)	94(2)	6.2(2.0)	b
NGC4448	bdbar	92(1)	0.67(0.01)	115(9)	0.07(0.01)	71(1)	24(1)	
NGC4450	bdbar	177(3)	0.33(0.03)	3.9(1.3)	0.46(0.01)	68(3)	27(3)	b
NGC4455	d	14(1)	0.64(0.01)	N/A	N/A	N/A	N/A	
NGC4457	bdbar	N/A	N/A	N/A	N/A	N/A	N/A	a
NGC4462	bdbar	122(1)	~ 0.65	133(2)	0.55(0.02)	53(3)	25(3)	
NGC4480	bd	174(1)	0.47(0.01)	N/A	N/A	96(1)	N/A	
NGC4487	dbar	75(3)	0.36(0.03)	101(1)	0.70(0.05)	96(1)	4(1)	
NGC4491	bdbar	145(1)	0.52(0.01)	122(2)	0.64(0.02)	80(2)	14(2)	
NGC4496A	dbar	35(5)	0.13(0.03)	56(2)	0.69(0.04)	89(2)	11(2)	
NGC4498	dbar	131(2)	0.55(0.02)	121(1)	0.86(0.02)	88(2)	12(2)	
NGC4501	bd	141(1)	0.54(0.01)	N/A	N/A	89(2)	N/A	
NGC4504	dbar	147(2)	0.41(0.03)	150(7)	0.09(0.04)	92(4)	8.1(3.5)	b
NGC4517A	dbar	N/A	N/A	N/A	N/A	N/A	N/A	a
NGC4519	dbar	131(6)	0.25(0.04)	68(2)	0.60(0.03)	86(2)	14(2)	
NGC4525	dbar	52(1)	0.48(0.02)	88(2)	0.66(0.02)	92(1)	8(1)	b
NGC4534	d	97(4)	0.29(0.04)	N/A	N/A	N/A	N/A	c
NGC4535	bdbar	15(10)	0.21(0.05)	37(4)	0.58(0.07)	86(2)	10(2)	
NGC4536	bd	124(2)	0.36(0.10)	N/A	N/A	84(6)	N/A	
NGC4539	dbar	94(1)	0.71(0.01)	103(3)	0.59(0.02)	85(2)	15(2)	b
NGC4545	d	22(3)	0.40(0.05)	N/A	N/A	N/A	N/A	b
NGC4548	bdbar	139(3)	0.26(0.02)	66(3)	0.43(0.03)	64(4)	30(3)	
NGC4559	dbar	143(1)	0.60(0.01)	120(4)	0.44(0.04)	92(1)	8.3(1.3)	b
NGC4562	d	53(1)	0.65(0.01)	N/A	N/A	N/A	N/A	c
NGC4569	bdbar	20(1)	0.59(0.03)	19(1)	0.75(0.02)	58(5)	20(4)	e
NGC4571	d	44(3)	0.13(0.01)	N/A	N/A	N/A	N/A	b c
NGC4579	bdbar	89(3)	0.21(0.02)	57(1)	0.63(0.04)	83(2)	12(2)	
NGC4580	bd	152(1)	0.32(0.01)	N/A	N/A	97(1)	N/A	
NGC4586	bd	114(1)	0.74(0.01)	N/A	N/A	65(2)	N/A	
NGC4602	bd	105(2)	0.61(0.02)	N/A	N/A	99(1)	N/A	
NGC4606	bdbar	26(1)	0.20(0.11)	40(1)	0.54(0.02)	25(6)	70(6)	
NGC4632	dbar	~ 60	~ 0.49	N/A	N/A	N/A	N/A	d
NGC4633	d	43(4)	0.54(0.05)	N/A	N/A	N/A	N/A	b
NGC4635	d	184(15)	0.19(0.09)	N/A	N/A	N/A	N/A	b
NGC4639	bdbar	144(4)	0.21(0.02)	166(1)	0.44(0.03)	59(4)	37(4)	
NGC4651	bd	76(2)	0.35(0.02)	N/A	N/A	99(1)	N/A	c
NGC4654	dbar	N/A	N/A	N/A	N/A	N/A	N/A	a
NGC4668	dbar	N/A	N/A	N/A	N/A	N/A	N/A	a c
NGC4682	bd	~ 90	~ 0.5	N/A	N/A	N/A	N/A	d
NGC4688	dbar	142(28)	0.07(0.05)	36(2)	~ 0.7	93(1)	6.5(1.0)	
NGC4689	bd	155(3)	0.22(0.02)	N/A	N/A	94(2)	N/A	
NGC4691	dbar	79(4)	0.45(0.05)	91(1)	0.80(0.01)	75(3)	25(3)	
NGC4713	dbar	81(4)	0.25(0.02)	86(2)	0.83(0.05)	98(1)	2.4(1.1)	b
NGC4725	bdbar	~ 40	~ 0.42	~ 50	~ 0.57	~ 50	~ 40	e
NGC4736	bd	~ 100	~ 0.12	N/A	N/A	N/A	N/A	c d
NGC4750	bd	121(3)	0.26(0.02)	N/A	N/A	92(1)	N/A	c
NGC4772	bd	146(1)	0.72(0.03)	N/A	N/A	39(2)	N/A	
NGC4775	d	107(9)	0.16(0.04)	N/A	N/A	N/A	N/A	b
NGC4779	bdbar	54(4)	0.15(0.03)	6(1)	~ 0.6	59(2)	31(2)	
NGC4781	dbar	118(1)	0.57(0.01)	79(4)	0.58(0.06)	88(2)	12(2)	
NGC4795	bdbar	117(3)	0.40(0.03)	23(2)	0.37(0.05)	70(3)	21(2)	

Name (1)	Model (2)	Disk PA [°] (3)	ϵ Disk (4)	Bar PA [°] (5)	ϵ Bar (6)	Disk % (7)	Bar % (8)	flags (9)
NGC4808	dbar	129(1)	0.65(0.01)	124(3)	0.63(0.02)	92(2)	7.6(2.4)	
NGC4826	bd	111(1)	0.51(0.03)	N/A	N/A	59(10)	N/A	c
NGC4897	bdbar	162(4)	0.26(0.02)	181(1)	0.50(0.03)	58(4)	20(3)	
NGC4899	bd	11(3)	0.44(0.04)	N/A	N/A	97(1)	N/A	
NGC4900	dbar	N/A	N/A	N/A	N/A	N/A	N/A	a
NGC4904	dbar	18(6)	0.31(0.05)	133(1)	0.69(0.03)	75(3)	25(3)	
NGC4941	bdbar	10(1)	0.21(0.05)	17(1)	0.48(0.01)	27(5)	67(4)	b
NGC4948	dbar	N/A	N/A	N/A	N/A	N/A	N/A	a
NGC4948A	dbar	6.0(3.3)	0.55(0.03)	N/A	N/A	N/A	N/A	
NGC4951	d	83(2)	0.44(0.02)	N/A	N/A	N/A	N/A	b
NGC4965	bd	128(4)	0.08(0.08)	N/A	N/A	31(21)	N/A	
NGC5012	bd	11(2)	0.51(0.02)	N/A	N/A	85(1)	N/A	
NGC5033	bd	170(1)	0.61(0.01)	N/A	N/A	84(1)	N/A	c
NGC5054	bd	157(1)	0.33(0.01)	N/A	N/A	99(1)	N/A	
NGC5068	dbar	N/A	N/A	N/A	N/A	N/A	N/A	b f
NGC5085	bd	45(4)	0.26(0.03)	N/A	N/A	95(2)	N/A	
NGC5088	d	185(1)	0.62(0.01)	N/A	N/A	N/A	N/A	c
NGC5101	bdbar	N/A	N/A	N/A	N/A	N/A	N/A	a
NGC5112	dbar	114(4)	0.44(0.06)	126(2)	0.73(0.03)	92(1)	8.0(1.3)	
NGC5117	bdbar	N/A	N/A	N/A	N/A	N/A	N/A	a
NGC5134	bdbar	N/A	N/A	N/A	N/A	N/A	N/A	b f
NGC5147	dbar	123(4)	0.19(0.02)	15(1)	0.76(0.01)	95(1)	5(1)	b
NGC5169	d	98(2)	0.51(0.02)	N/A	N/A	N/A	N/A	b c
NGC5205	bdbar	109(1)	0.57(0.03)	157(2)	0.43(0.02)	31(3)	55(2)	
NGC5236	bdbar	~ 50	~ 0.19	N/A	N/A	N/A	N/A	d
NGC5240	d	47(5)	0.39(0.06)	N/A	N/A	N/A	N/A	b
NGC5247	bd	~ 10	~ 0.05	N/A	N/A	~ 90	N/A	e
NGC5248	d	119(3)	0.34(0.03)	N/A	N/A	N/A	N/A	b c
NGC5254	d	126(1)	0.56(0.01)	N/A	N/A	N/A	N/A	b
NGC5300	dbar	146(2)	0.36(0.01)	156(9)	0.34(0.07)	97(1)	3(1)	b
NGC5320	d	15(2)	0.45(0.02)	N/A	N/A	N/A	N/A	b
NGC5334	dbar	17(3)	0.27(0.02)	45(2)	0.63(0.03)	96(1)	4(1)	b
NGC5339	bdbar	52(7)	0.14(0.03)	85(2)	0.52(0.03)	68(3)	29(3)	
NGC5346	bd	161(1)	0.53(0.02)	N/A	N/A	89(3)	N/A	
NGC5364	d	42(3)	0.39(0.03)	N/A	N/A	N/A	N/A	b c
NGC5375	bdbar	179(2)	0.22(0.02)	169(1)	0.66(0.02)	82(2)	15(2)	b
NGC5377	bdbar	34(2)	0.43(0.05)	45(1)	0.67(0.02)	35(9)	39(4)	
NGC5383	dbar	76(2)	0.50(0.03)	131(2)	0.55(0.03)	54(4)	46(4)	b c
NGC5430	bdbar	18(2)	0.30(0.05)	151(2)	0.63(0.02)	59(3)	32(3)	
NGC5443	bdbar	219(2)	0.29(0.05)	40(1)	0.67(0.01)	27(4)	68(4)	
NGC5448	bdbar	109(2)	0.71(0.21)	98(2)	0.76(0.03)	29(6)	26(13)	
NGC5457	bd	84(9)	0.05(0.05)	N/A	N/A	67(16)	N/A	
NGC5468	bd	~ 160	~ 0.05	N/A	N/A	~ 80	N/A	e
NGC5534	bdbar	234(7)	0.30(0.04)	79(1)	0.76(0.03)	52(4)	15(3)	
NGC5566	bdbar	30(1)	0.59(0.03)	197(7)	0.18(0.04)	52(4)	44(3)	
NGC5569	dbar	67(7)	0.24(0.05)	73(2)	0.74(0.05)	97(1)	3(1)	
NGC5585	bd	31(2)	0.41(0.03)	N/A	N/A	88(2)	N/A	
NGC5597	dbar	-132(3)	0.52(0.03)	29(1)	0.88(0.03)	94(1)	5.7(1.0)	
NGC5602	bd	166(1)	0.48(0.01)	N/A	N/A	57(2)	N/A	
NGC5604	d	7(1)	~ 0.44	N/A	N/A	N/A	N/A	b c
NGC5630	dbar	96(3)	0.61(0.04)	115(1)	0.83(0.03)	82(3)	18(3)	
NGC5645	dbar	92(7)	0.42(0.06)	135(2)	0.69(0.03)	89(2)	11(2)	
NGC5660	bd	56(21)	0.11(0.06)	N/A	N/A	90(3)	N/A	
NGC5668	d	118(10)	0.10(0.03)	N/A	N/A	N/A	N/A	c
NGC5669	dbar	58(51)	0.14(0.08)	48(2)	0.62(0.02)	95(1)	5.2(1.4)	
NGC5676	bd	43(1)	0.51(0.02)	N/A	N/A	94(3)	N/A	
NGC5678	d	-1(2)	0.36(0.02)	N/A	N/A	N/A	N/A	b
NGC5693	dbar	289(18)	0.12(0.05)	56(3)	0.67(0.04)	91(2)	8.9(1.8)	
NGC5713	bdbar	-285(65)	0.08(0.03)	101(2)	0.61(0.03)	69(4)	29(4)	
NGC5719	dbar	N/A	N/A	N/A	N/A	N/A	N/A	a b

Name (1)	Model (2)	Disk PA [°] (3)	ϵ Disk (4)	Bar PA [°] (5)	ϵ Bar (6)	Disk % (7)	Bar % (8)	flags (9)
NGC5728	bdbar	8.9(5.0)	0.28(0.03)	34(1)	0.63(0.01)	36(4)	50(3)	
NGC5740	bdbar	158(1)	0.50(0.01)	138(4)	0.41(0.03)	64(3)	21(3)	
NGC5750	bdbar	~ 60	~ 0.4	~ 100	~ 0.26	~ 70	~ 30	b e
NGC5756	dbar	49(2)	0.48(0.03)	36(2)	0.72(0.03)	65(9)	35(9)	b
NGC5757	bdbar	13(9)	0.20(0.07)	162(2)	0.72(0.04)	69(5)	18(4)	
NGC5762	bd	118(2)	0.09(0.01)	N/A	N/A	87(1)	N/A	c
NGC5774	dbar	101(2)	0.45(0.03)	40(11)	0.35(0.03)	85(3)	15(3)	c
NGC5783	d	171(7)	0.30(0.07)	N/A	N/A	N/A	N/A	b
NGC5806	bdbar	170(1)	0.51(0.01)	174(1)	0.64(0.02)	68(6)	20(6)	
NGC5832	dbar	39(2)	0.32(0.03)	194(3)	0.19(0.02)	63(2)	37(2)	b
NGC5850	bdbar	224(2)	0.05(0.01)	120(1)	0.54(0.03)	60(3)	34(3)	
NGC5861	d	158(2)	0.41(0.03)	N/A	N/A	N/A	N/A	b
NGC5878	bdbar	4(1)	~ 0.66	169(3)	0.52(0.02)	72(1)	8.7(1.6)	
NGC5879	d	4(1)	0.64(0.01)	N/A	N/A	N/A	N/A	b c
NGC5892	dbar	232(13)	0.15(0.05)	159(2)	0.65(0.04)	97(1)	3(1)	
NGC5899	dbar	23(2)	0.65(0.02)	142(5)	0.60(0.07)	90(2)	10(2)	b
NGC5913	dbar	166(2)	0.53(0.02)	31(3)	0.57(0.03)	73(3)	27(3)	b
NGC5949	d	143(1)	0.55(0.01)	N/A	N/A	N/A	N/A	b
NGC5957	bdbar	94(3)	0.35(0.03)	N/A	N/A	96(1)	N/A	c
NGC5962	bd	127(6)	0.33(0.06)	N/A	N/A	89(3)	N/A	c
NGC5964	dbar	N/A	N/A	N/A	N/A	N/A	N/A	a
NGC5970	dbar	90(2)	0.40(0.02)	74(1)	0.76(0.02)	91(2)	9.1(1.6)	b
NGC6015	d	31(2)	0.47(0.01)	N/A	N/A	N/A	N/A	b
NGC6070	bd	~ 60	~ 0.51	N/A	N/A	~ 90	N/A	e
NGC6118	bd	54(1)	0.57(0.02)	N/A	N/A	98(1)	N/A	
NGC6207	d	N/A	N/A	N/A	N/A	N/A	N/A	c f
NGC6217	dbar	147(3)	0.52(0.07)	46(1)	0.78(0.02)	95(3)	5.4(2.9)	b
NGC6236	dbar	9.9(5.4)	0.34(0.06)	81(28)	0.42(0.15)	99(1)	1(1)	
NGC6237	dbar	147(2)	0.42(0.03)	163(1)	0.78(0.03)	83(3)	17(3)	
NGC6255	dbar	83(1)	0.60(0.02)	95(1)	0.78(0.01)	81(2)	19(2)	
NGC6339	dbar	-9(10)	0.31(0.10)	108(1)	0.74(0.01)	83(1)	17(1)	
NGC6395	bd	17(1)	0.68(0.02)	N/A	N/A	90(6)	N/A	
NGC6902	bd	152(1)	0.22(0.01)	N/A	N/A	90(1)	N/A	c
NGC6923	bdbar	N/A	N/A	N/A	N/A	N/A	N/A	a
NGC6925	bdbar	6(1)	~ 0.72	128(15)	0.07(0.02)	70(1)	21(1)	
NGC7059	dbar	105(4)	0.37(0.05)	152(7)	0.25(0.03)	92(2)	8.0(1.8)	
NGC7070	dbar	25(5)	0.31(0.04)	85(3)	0.64(0.03)	97(1)	3(1)	
NGC7091	dbar	74(5)	0.37(0.04)	89(1)	0.77(0.03)	92(2)	8.2(2.4)	
NGC7098	bdbar	67(2)	0.27(0.02)	52(1)	0.49(0.02)	57(3)	39(3)	b
NGC7140	bdbar	15(1)	0.40(0.04)	19(1)	0.67(0.02)	61(5)	35(4)	
NGC7151	d	82(2)	0.58(0.04)	N/A	N/A	N/A	N/A	b
NGC7162	bd	13(1)	0.64(0.03)	N/A	N/A	82(8)	N/A	
NGC7163	bdbar	102(1)	0.55(0.02)	72(8)	0.50(0.10)	74(2)	3.6(1.9)	
NGC7171	bd	118(3)	0.51(0.02)	N/A	N/A	95(2)	N/A	
NGC7188	dbar	47(1)	0.52(0.01)	138(2)	0.54(0.01)	95(1)	5(1)	b
NGC7205	bd	67(2)	0.49(0.02)	N/A	N/A	96(1)	N/A	
NGC7218	dbar	31(2)	0.48(0.03)	97(1)	0.55(0.01)	86(1)	14(1)	b
NGC7219	bd	66(4)	0.24(0.03)	N/A	N/A	85(1)	N/A	c
NGC7418	dbar	131(6)	0.41(0.04)	N/A	N/A	N/A	N/A	b e
NGC7421	bdbar	70(10)	0.10(0.03)	90(1)	0.72(0.03)	90(1)	9.0(1.3)	
NGC7424	dbar	82(23)	0.18(0.07)	132(1)	0.60(0.02)	94(1)	6(1)	
NGC7437	bd	50(27)	0.10(0.05)	N/A	N/A	100(1)	N/A	
NGC7456	d	24(1)	0.63(0.01)	N/A	N/A	N/A	N/A	b
NGC7479	bdbar	37(13)	0.27(0.08)	6(1)	0.82(0.02)	68(4)	27(4)	
NGC7513	bdbar	99(4)	0.30(0.05)	71(1)	0.77(0.02)	77(3)	21(3)	
NGC7531	bdbar	18(1)	0.37(0.03)	14(1)	0.59(0.01)	46(5)	53(5)	
NGC7590	bd	30(1)	0.60(0.01)	N/A	N/A	91(1)	N/A	
NGC7599	dbar	N/A	N/A	N/A	N/A	N/A	N/A	a
NGC7606	bd	145(1)	0.58(0.01)	N/A	N/A	94(1)	N/A	
NGC7661	dbar	23(3)	0.32(0.03)	50(1)	0.73(0.03)	90(2)	9.9(2.5)	

Name (1)	Model (2)	Disk PA [°] (3)	ϵ Disk (4)	Bar PA [°] (5)	ϵ Bar (6)	Disk % (7)	Bar % (8)	flags (9)
NGC7689	d	126(7)	0.29(0.07)	N/A	N/A	N/A	N/A	b
NGC7713	dbar	N/A	N/A	N/A	N/A	N/A	N/A	a
NGC7721	bd	16(1)	~ 0.64	N/A	N/A	86(4)	N/A	
NGC7723	bdbar	43(2)	0.29(0.02)	70(1)	0.75(0.02)	85(2)	8(1)	
NGC7755	bdbar	27(1)	0.18(0.01)	122(2)	0.35(0.02)	75(2)	24(2)	
NGC7757	dbar	99(3)	0.44(0.05)	32(24)	0.05(0.01)	71(5)	29(5)	b
NGC7793	d	94(4)	0.29(0.04)	N/A	N/A	N/A	N/A	b
NGC7817	bd	47(1)	0.76(0.01)	N/A	N/A	94(1)	N/A	
PGC003853	dbar	102(4)	0.20(0.02)	39(1)	~ 0.63	94(1)	6(1)	
PGC006190	d	170(1)	0.69(0.01)	N/A	N/A	N/A	N/A	c
PGC006667	dbar	99(48)	0.05(0.04)	51(4)	0.62(0.02)	93(1)	6.7(1.3)	
PGC009559	d	N/A	N/A	N/A	N/A	N/A	N/A	c f
PGC011248	dbar	121(1)	0.59(0.02)	90(1)	0.73(0.02)	81(2)	19(2)	
PGC011367	bd	N/A	N/A	N/A	N/A	N/A	N/A	f
PGC012664	dbar	152(7)	0.27(0.06)	91(1)	0.71(0.01)	95(1)	5(1)	
PGC013716	d	139(1)	~ 0.69	N/A	N/A	N/A	N/A	b
PGC014487	d	131(4)	0.28(0.03)	N/A	N/A	N/A	N/A	c
PGC014768	dbar	165(1)	0.63(0.02)	147(9)	0.34(0.05)	87(2)	13(2)	
PGC027616	dbar	-42(5)	0.26(0.03)	106(2)	0.63(0.03)	96(1)	4(1)	
PGC027825	dbar	144(3)	0.57(0.03)	124(3)	0.67(0.03)	90(2)	10(2)	
PGC027833	dbar	95(14)	0.09(0.04)	98(3)	0.78(0.06)	99(1)	1(1)	
PGC028380	dbar	60(5)	0.34(0.05)	112(2)	0.71(0.05)	88(2)	12(2)	
PGC031979	bd	240(6)	0.05(0.03)	N/A	N/A	81(11)	N/A	
PGC036217	dbar	9(18)	0.28(0.09)	166(2)	0.66(0.05)	95(2)	4.7(1.8)	b
PGC036551	d	71(1)	0.62(0.01)	N/A	N/A	N/A	N/A	
PGC042068	bd	34(1)	0.32(0.05)	N/A	N/A	46(18)	N/A	b
PGC045195	dbar	52(5)	0.30(0.05)	82(3)	0.54(0.07)	92(3)	8.0(2.8)	
PGC045824	d	68(2)	0.57(0.03)	N/A	N/A	N/A	N/A	c
PGC047721	dbar	N/A	N/A	N/A	N/A	N/A	N/A	a b
PGC050229	d	152(1)	0.45(0.01)	N/A	N/A	N/A	N/A	b c
PGC053415	d	50(1)	~ 0.56	N/A	N/A	N/A	N/A	c
PGC053779	dbar	89(2)	0.37(0.02)	69(2)	0.50(0.02)	82(4)	18(4)	c
PGC066242	dbar	41(1)	0.54(0.01)	17(1)	0.75(0.03)	94(1)	6(1)	
PGC067871	dbar	154(8)	0.37(0.08)	49(2)	0.61(0.02)	86(2)	14(2)	
PGC068771	dbar	59(41)	0.12(0.08)	33(3)	0.71(0.06)	94(2)	6.0(1.6)	
PGC069448	d	70(6)	0.41(0.08)	N/A	N/A	N/A	N/A	b
UGC00132	d	14(1)	0.66(0.01)	N/A	N/A	N/A	N/A	
UGC01551	dbar	130(5)	0.14(0.02)	82(2)	0.56(0.04)	91(1)	9.2(1.3)	b
UGC01862	dbar	~ -10.38	~ 0.14	N/A	N/A	N/A	N/A	e
UGC02081	bd	70(2)	0.43(0.03)	N/A	N/A	96(1)	N/A	
UGC04169	d	136(2)	0.45(0.03)	N/A	N/A	N/A	N/A	
UGC04390	dbar	83(4)	0.21(0.03)	52(2)	0.64(0.03)	93(1)	7.4(1.0)	
UGC04514	dbar	67(2)	0.58(0.03)	77(1)	0.86(0.03)	85(5)	15(5)	
UGC04543	d	-27(6)	0.34(0.05)	N/A	N/A	N/A	N/A	c
UGC04701	d	147(7)	0.22(0.06)	N/A	N/A	N/A	N/A	c
UGC04787	d	7(1)	0.64(0.02)	N/A	N/A	N/A	N/A	
UGC04841	dbar	131(4)	0.32(0.04)	17(4)	0.57(0.05)	97(1)	2.8(1.0)	
UGC05015	d	29(3)	0.20(0.02)	N/A	N/A	N/A	N/A	c
UGC05179	bd	110(3)	0.31(0.06)	N/A	N/A	90(5)	N/A	
UGC05228	dbar	122(1)	0.70(0.01)	116(1)	0.83(0.01)	87(4)	13(4)	b
UGC05238	dbar	N/A	N/A	N/A	N/A	N/A	N/A	a
UGC05354	dbar	78(2)	0.45(0.03)	53(3)	0.64(0.01)	94(1)	6.1(1.2)	
UGC05358	dbar	78(2)	0.67(0.03)	107(1)	0.73(0.03)	77(3)	23(3)	
UGC05707	dbar	221(10)	0.29(0.06)	67(1)	0.73(0.03)	95(1)	5(1)	
UGC05897	bd	72(1)	0.67(0.01)	N/A	N/A	89(3)	N/A	
UGC05976	d	42(5)	0.23(0.04)	N/A	N/A	N/A	N/A	c
UGC06157	dbar	-6(6)	0.33(0.04)	145(2)	0.59(0.05)	88(3)	12(3)	
UGC06162	bd	93(3)	0.47(0.03)	N/A	N/A	96(1)	N/A	
UGC06249	d	49(5)	0.22(0.03)	N/A	N/A	N/A	N/A	c
UGC06335	bd	136(13)	0.16(0.05)	N/A	N/A	93(1)	N/A	

Name (1)	Model (2)	Disk PA [°] (3)	ϵ_{Disk} (4)	Bar PA [°] (5)	ϵ_{Bar} (6)	Disk % (7)	Bar % (8)	flags (9)
UGC06446	d	28(9)	0.10(0.03)	N/A	N/A	N/A	N/A	c
UGC06879	dbar	168(1)	0.68(0.01)	110(3)	0.52(0.03)	95(1)	5(1)	
UGC06903	dbar	122(9)	0.31(0.06)	100(1)	0.67(0.01)	96(1)	4(1)	
UGC06922	d	57(2)	0.21(0.01)	N/A	N/A	N/A	N/A	c
UGC06983	dbar	N/A	N/A	N/A	N/A	N/A	N/A	a
UGC07133	dbar	176(3)	0.46(0.04)	92(6)	0.56(0.02)	96(1)	4(1)	
UGC07267	d	51(1)	0.64(0.02)	N/A	N/A	N/A	N/A	
UGC07271	d	162(1)	0.53(0.02)	N/A	N/A	N/A	N/A	c
UGC07700	dbar	91(6)	0.43(0.06)	89(1)	0.94(0.01)	92(1)	8.4(1.4)	
UGC07848	d	65(2)	0.52(0.04)	N/A	N/A	N/A	N/A	b
UGC08041	dbar	165(1)	0.50(0.02)	80(6)	0.46(0.08)	93(1)	6.8(1.4)	b
UGC08056	bdbar	168(2)	0.44(0.02)	170(1)	0.60(0.02)	77(5)	20(4)	
UGC08153	bd	-50(4)	0.05(0.05)	N/A	N/A	85(6)	N/A	
UGC08155	bd	287(18)	0.05(0.01)	N/A	N/A	85(4)	N/A	
UGC08313	d	35(1)	0.70(0.01)	N/A	N/A	N/A	N/A	
UGC08365	dbar	105(1)	0.48(0.02)	115(1)	0.79(0.03)	78(3)	22(3)	
UGC08597	dbar	N/A	N/A	N/A	N/A	N/A	N/A	f
UGC08658	dbar	110(5)	0.39(0.04)	119(14)	0.42(0.04)	93(3)	6.6(2.6)	b
UGC08733	dbar	3.7(3.4)	0.55(0.03)	153(4)	0.57(0.05)	95(1)	5(1)	
UGC08995	dbar	3.6(1.1)	0.62(0.02)	143(7)	0.51(0.05)	96(1)	4(1)	
UGC09057	dbar	182(1)	0.74(0.02)	160(1)	0.69(0.02)	89(1)	11(1)	
UGC09215	dbar	153(8)	0.45(0.08)	112(1)	0.70(0.01)	80(2)	20(2)	
UGC09245	dbar	202(3)	0.42(0.05)	16(1)	0.79(0.01)	82(2)	18(2)	
UGC09274	d	50(2)	0.54(0.03)	N/A	N/A	N/A	N/A	
UGC09299	dbar	84(5)	0.48(0.05)	106(2)	0.68(0.04)	93(3)	6.6(3.0)	
UGC09394	bd	42(1)	0.76(0.02)	N/A	N/A	94(1)	N/A	
UGC09837	bd	216(7)	0.05(0.05)	N/A	N/A	96(1)	N/A	
UGC09951	d	~ 120	~ 0.36	N/A	N/A	N/A	N/A	c d
UGC10020	d	N/A	N/A	N/A	N/A	N/A	N/A	c f
UGC10437	d	167(4)	0.18(0.03)	N/A	N/A	N/A	N/A	c
UGC10445	bd	124(3)	0.32(0.03)	N/A	N/A	98(2)	N/A	
UGC12707	dbar	43(3)	0.46(0.03)	65(2)	0.72(0.03)	86(2)	14(2)	b

Table A1: Galaxies in S⁴G subsample. Column 1 is the galaxy name, column 2 indicates the model used in DISKFIT (b=bulge, d=disk, and bar), column 3 is the position angle of the disk in degrees (numbers in parentheses are the uncertainties on the reported values), column 4 is the ellipticity of the disk ($1 - b/a$), column 5 is the position angle of the bar in degrees, column 6 is the bar ellipticity, column 7 is the fraction of the model light in the disk, column 8 is the fraction of the model light in the bar, and column 9 is the fit flag. The fit flags are a: Excluded galaxies with $|PA_{\text{Disk}} - PA_{\text{Bar}}| < 5^\circ$. b: Nucleus included in GALFIT fit, but not in DISKFIT fit. c: Two disks fit in GALFIT, one disk fit in DISKFIT. d: Galaxies for which the only model that we could fit was disk-only, with fewer surface brightness rings than used in other DISKFIT fits. e: Galaxies for which we fit the same components as in the GALFIT fits, with fewer surface brightness rings than used in other DISKFIT fits. f: Galaxies for which GALFIT parameters used as DISKFIT inputs caused DISKFIT minimization to fail.